Ore Geology Reviews 140 (2022) 104557

Contents lists available at ScienceDirect

Ore Geology Reviews

journal homepage: www.elsevier.com/locate/oregeorev

Genesis of interlayer oxidation zone-type uranium deposit in the channel conglomerates, Beisantai area, Junggar Basin: An insight into uranium mineralization

Xiaowen Hu [a,b], Xiaoyong Yang [a,b,*], Yisu Ren [a,b,*], Gaofeng Du [c], Zhaojian Wu [d]

[a] CAS Key Laboratory of Crust-Mantle Materials and Environments, University of Science and Technology of China, Hefei 230026, China
[b] CAS Center for Excellence in Comparative Planetology, University of Science and Technology of China, Hefei 230026, China
[c] Key Laboratory for Digital Land and Resources of Jiangxi Province, East China University of Technology, Nanchang 330013, China
[d] China Coal Geology Group Co, Ltd, Beijing 100040, China

ARTICLE INFO

Keywords:
Interlayer oxidation zone
Uranium mineralization
Calcite cement
Pyrite
Microbes
Junggar Basin

ABSTRACT

The Beisantai deposit is a newly discovered typical interlayer oxidation zone-type uranium deposit mainly hosted in distributary channel conglomerates of the Neogene Shawan Formation in East Junggar Basin, northwest China. This study aims to reveal the genetic process of the Beisantai deposit and constrain the mineralization characteristics conducted through petrographic observation, Rock-Eval pyrolysis, high-resolution microscopic mineralogical observation based on BSE, C-O isotopes of calcite cement, and *in-situ* measurements on pyrite of trace elements and S isotope. There are two types of calcite cements, including diagenetic microcrystalline calcite and epigenetic sparry calcite, dominantly occurring in the redox transition zone and the oxidation zone, respectively. The broad heterogeneity of $\delta^{13}C$ values, ranging from −29.2‰ to −6.52‰, indicates the mixed sources of carbon. Given the poor organic content in sediments (0.05% in sandstone and from 0.11% to 0.26% in mudstones), the large amount of organic carbon in the transition zone conglomerates, revealed by the super low $\delta^{13}C$ values, is attributed to extrinsic hydrocarbons. Besides, the widespread dissolution of microcrystalline calcite also indicates a weakly acidic environment in the formation. The heavy carbon isotopes are sourced from surface freshwater and the dissolved CO_2, which causes the epigenetic metasomatism of early-stage calcite. Thus, the infiltrated groundwater is characterized as alkaline with carbonate dissolved. Pyrites are highly enriched in ore-bearing rocks, with complex morphologies. The extremely negative sulfur isotopic signatures ($\delta^{34}S$ values from −48.38‰ to −35.65‰) indicate that these pyrites precipitate through bacterial sulfate reduction (BSR). Combined with the morphology features, distribution patterns, and the decrease in light sulfur isotope and several trace elements, including As, Se, Ni, and Co between individual pyrites and ore-related pyrites, a successive process of pyritization can be revealed. Ore-related pyrites are formed at the late stage. The pervasive coffinite replacement of pyrite suggests that uranium mineralization should occur after the cessation of pyritization, resulting from the consumption of organic matter. Distinctive bio-oxidation features of pyrite can also be observed, characterized as deep and oriented holes. Thus the role of microbes such as *Acidithiobacillus thiooxidans* is non-negligible, which enhances the dissolution rate of pyrite and the reduction of U(VI). Overall, as the major reducing material during the ore stage, the large amount of pyrite has played the predominant role in the precipitation of coffinite, with the catalysis and acceleration of microbes.

1. Introduction

Sandstone-type uranium deposits, mainly occurring in permeable sandstone, pebbly sandstone, or conglomerate, generally originated in the supergene low-temperature fluid environment (Kyser, 2014; Zhao et al., 2020), have attracted increasing attention for its cost-efficiency with the development of *in-situ* leaching technology in recent years (OECD-NEA-IAEA, 2020). Genesis of sandstone-type uranium deposits in interlayer oxidation zone is globally modeled as U transported by oxidising groundwater within permeable layers down dip to the redox

* Corresponding authors at: CAS Key Laboratory of Crust-Mantle Materials and Environments, University of Science and Technology of China, Hefei 230026, China.
E-mail addresses: xyyang@ustc.edu.cn (X. Yang), renyisu@mail.ustc.edu.cn (Y. Ren).

https://doi.org/10.1016/j.oregeorev.2021.104557
Received 23 April 2021; Received in revised form 20 October 2021; Accepted 28 October 2021
Available online 3 November 2021
0169-1368/© 2021 Published by Elsevier B.V. This is an open access article under the CC BY-NC-ND license (http://creativecommons.org/licenses/by-nc-nd/4.0/).

front, where soluble U (VI) is reduced to insoluble U (IV) by reductants such as carbonaceous materials, sulfides, and hydrocarbons (Curiale et al., 1983; Hansley and Spirakis, 1992; Spirakis, 1996; Kyser, 2014, 2016). The mineralization processes, including complex Physico-chemical interactions, adsorption, and microbial activities, are hard to constrain despite numerous studies that have been conducted for decades.

According to the origin, the reducing materials can be subdivided into (1) intrinsic reductants, in primary regionally reduced sandstones; (2) extrinsic reductants such as oil & gas that are introduced into reservoirs devoid of inherited organic matter (OM); and (3) a combination of both sources above (Bonnetti et al., 2020). In any case, organic matter is considered to be the major reductant in the formation. In these deposits, it is broadly observed that uranium minerals are intimately intergrown with pyrites which show very light sulfur isotope signatures, attributed to sulfate-reducing bacteria (SRB; Southam and Saunders, 2005). Organic matter has usually been replaced by ore-stage pyrite or uranium minerals but without substitution relation between them (e.g. Bonnetti et al., 2017; Zhao et al., 2018; Chen et al., 2019), suggesting that they may precipitate simultaneously or successively in a short time and be triggered by the same mechanism. It can be interpreted that SRB is capable of utilizing organic matter as nutriment and reduce sulfates to sulfides, with the reduction of U(VI) to U(IV) simultaneously (Lovley and Phillips, 1992; Lovley et al., 1993; Abdelouas et al., 1998). Thus, the role of SRB has been emphasized in sandstone-type deposits in recent years. Although the reductant role of pyrite has also been mentioned in some deposits (Jaireth et al., 2008; Yue et al., 2019), it is the secondary factor thus with less attention paid. Overall, organic matter commonly acts as the predominant reductant in the organic matter-rich sandstone-type uranium reservoirs, resulting in the precipitation of pyrite and uranium minerals and protecting them from oxidation.

The newly discovered Beisantai deposit occurs in conglomerates short of OM. Uranium minerals are also closely associated with pyrites. However, these pyrites are pervasively corroded and replaced by post-dated uranium minerals. Indeed, uptake and reduction of U(VI) by pyrite under acidic conditions have been manifested depending on plenty of laboratory work (Wersin et al., 1994; Eglizaud et al., 2006; Scott et al., 2007; Gallegos et al., 2015; Ma et al., 2020). Besides, some experiments have also focused on microbially mediated reduction of uranium such as *Acidithiobacillus ferrooxidans* and *Acidithiobacillus thiooxidans* that are able to reduce U(VI) based on pyrite (Pisapia et al., 2008; Gargarello et al., 2009; 2010; Jiang et al., 2011; Zhang et al., 2020). Biotic controlled oxidation is identified to increase the pyrite dissolution rates by several orders of magnitude (Sampson et al., 2000; Crundwell, 2003; Pisapia et al., 2008; Yin et al., 2020) and has been applied to the bio-leaching of sulfide minerals in mining operations (Gleisner et al., 2006; Zhao et al., 2013) as well as U-containing water/sediments remediation (Borch et al., 2012; Larson et al., 2012). Nevertheless, it is seldom reported in literature about uranium ore deposits. In the Beisantai deposit, many phenomena in the corroded pyrites can be involved in bio-oxidation. Given this, it is necessary to re-estimate the significance of pyrite in the precipitation of uranium as well as its role during the formation of sandstone-type deposits.

The purpose of this paper is based on the Beisantai deposit, mainly from the mineralogical and geochemical studies of organic matter, calcite cement, pyrite, and uranium minerals, trying to reveal its genesis and demonstrating for the first time uranium mineralization through the predominant reduction of pyrite with the promotion of biotic pathways, under the condition of lack of organic matter.

2. Geological setting

2.1. Junggar Basin

The Junggar Basin, located in the north part of the Xinjiang Uygur Autonomous Region, northwest China (Fig. 1A), covering an area of approximately 130,000 km^2, is a giant superimposed Meso-Cenozoic basin with abundant resources (Allen et al., 1995; Cai et al., 2000; Chen et al., 2002; Yang et al., 2015). The basin is surrounded by Zhayier Mountains and Hatealate Mountains to the west, Qinggelidi Mountains and Kelameili Mountains to the east, and Yilinheibiergen Mountains and Bogda Mountains to the south (Fig. 1B), which are composed of

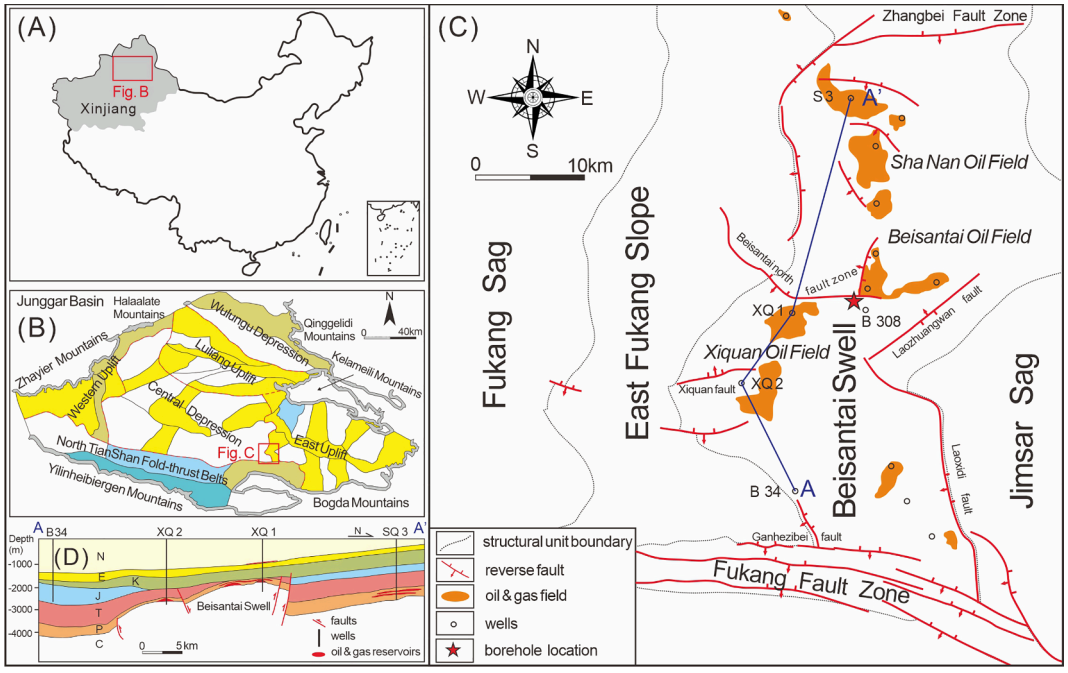


Fig. 1. Geological map and cross-section of the Beisantai area. (A) Map of China, the Junggar Basin locates in northwestern China. (B) Structural units of the Junggar Basin (modified after Yang et al., 2004) showing the location of the study area. (C) Regional geological map of the Beisantai area showing the sampling location (modified after Zhang, 2016). (D) North-South cross-section AA' cross the Beisantai Swell revealed by seismic tomography and drilling wells (modified after Zhang, 2016).

Paleozoic ophiolites, accretionary sedimentary rocks, and island arc volcanics (Carroll et al., 1990; Xiao et al., 2008) that provide a great deal of material for the sedimentary basin. During the Mesozoic and the Cenozoic, the basin has been subjected to the Indosinian, Yenshanian, and Himalayan orogenies (Wu, 1986; Luo et al., 2012; Sun et al., 2014; Hu et al., 2020). It can be subdivided into six major structural units (Fig. 1B): the Western Uplift, the Wulungu Depression, the Luliang Uplift, the Central Depression, the East Uplift, and the North TianShan Fold-thrust Belts (Yang et al., 2004).

2.2. Beisantai deposit

The Beisantai area is a paleo-swell that formed in the late Hercynian, developed in the Indosinian, and finalized in the Yansanian (Wu et al., 2012). During the Himalayas, the south margin was in a rejuvenated foreland basin environment, where the strata had undergone strong compression and strike-slipping deformation. Under the condition of flexural subsidence that the basement sloped towards the south, the Cenozoic in the Beisantai area covered a thickness of more than 2000 m (Wu et al., 2004). With the lake transgression, the sedimentary environment in Neogene, including the Shawan Formation (N_1s), Taxihe Formation (N_1t), and Dushanzi Formation (N_1d), had evolved from delta to lacustrine, from which the Shawan Formation was identified as delta facies.

Since the climate has become arid from the Neogene (Yang and He, 2016), the Shawan Formation is dominated by reddish-brown argillaceous siltstones and mudstones; the Taxihe Formation is dominated by brown–red sandy conglomerates; the Dushanzi Formation is mainly composed of interbedded brownish-yellow sandy mudstones, conglomerates, and sandstones. A number of oil fields have been discovered in the Beisantai area, e.g. Shanan oil field, Beisantai oil field, and Xiquan oil field from north to south (Wu et al., 2012). Intense tectonic activities during Yanshanian and Himalayan lead to fault reactivation and petroleum migration repeatedly (Pan, 2007; Wu et al., 2012). Some oil and gas shows were also found in shallow layers (including the Paleogene and the Neogene) of Beisantai Swell (Zhao et al., 2016).

The newly discovered Beisantai uranium deposit is due to the pioneering work "co-exploration of petroleum and uranium" of the ongoing "survey of sandstone-type uranium in northern China" (Jin et al., 2018; Miao et al., 2020). Based on the recheck of a huge amount of data from oil boreholes, the promising positions are selected, where show high radioactive anomalies. The Beisantai deposit is located in the Beisantai Swell, west margin of East Uplift, next to the East Fukang Slope, about 100 km to the northeast of Urumchi City (Fig. 1C). This deposit is situated on a southwesterly sloping monocline (Fig. 1D) nearby the EW orientation of a major reverse fault in the north, which controls the formation of the Beisantai oil field (Wu et al., 2012). A borehole was performed at the Beisantai Swell located between the Beisantai oil field

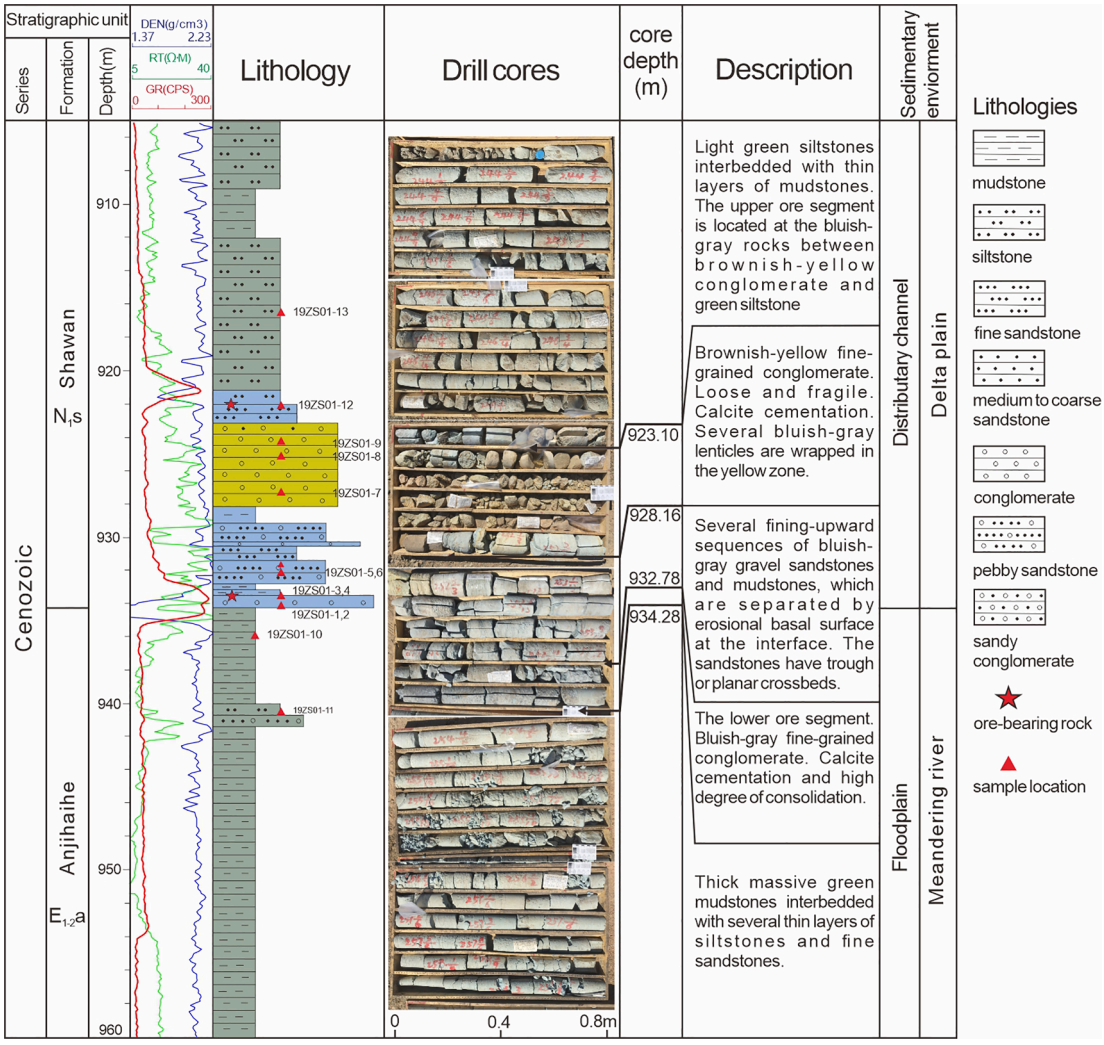


Fig. 2. Sedimentological characteristics of the uranium borehole of the Beisantai deposit, showing the logging curves, lithology, cores, and sedimentary environment of the top of Anjihaihe Formation and the bottom of Shawan Formation.

and the Xiquan oil field. The uranium deposit is hosted in the bottom of the Neogene Shawan Formation that is mainly composed of conglomerates and gravel pebbly sandstones, at a depth around 950 m below the surface, with 12 m permeable rocks. The reservoir is sandwiched by super thick impermeable formations, mainly mudstones and siltstones, providing a favorable structure for the formation of interlayer oxidation zone (Fig. 2).

Controlled by interlayer drainage of oxidising groundwater, there is an obvious brownish-yellow oxidation zone in the middle part, in which the rocks are loose and fragile (Fig. 2). The adjacent bluish-gray sandstones and conglomerates, representing the redox transition zone, are separated into several individual drainage systems by thin interlayers of mudstones, thus showing different degrees of epigenetic alteration (Fig. 2). Uranium minerals are mainly observed in the bluish-gray conglomerates at the bottom of the Shawan Formation (Fig. 2; Table 1), showing a higher radioactive anomaly (Fig. 2; Table 1), with a great deal of pyrites occurred.

3. Sampling and methods

The samples were collected from a borehole in the Beisantai deposit, southeast of Junggar Basin. Centered on the bottom of the Neogene Shawan Formation, fifteen cores were selected from different color zones (Fig. 2; Table. 1). During collection, the γ-ray responses were measured for rough potential estimation with a gamma radiometer and all of them were sealed in plastic bags, in order to prevent from humid air and oxidation before geochemical/mineralogical study.

The mineralogical study was performed using optical microscope (transmitted-reflected lights and fluorescence) and scanning electron microscopy (SEM) in the Key Laboratory of Crust-Mantle Materials and Environments, University of Science and Technology of China, Chinese Academy of Sciences. A MIRA 3 LMH (FE-SEM) was used to take BSE images and equipped with EDAX GENESIS APEX to identify minerals and perform compositional X-ray maps. This measurement was carried out under an accelerating voltage of 15 kV, a beam current of 20nA on polished sections in situ. Organic matter typology and maturity were determined by rock–eval VI pyrolysis at Guangzhou Institute of Geochemistry, Chinese Academy of Sciences.

Ten samples from different zones were selected for carbon and oxygen isotope analyses at the ALS Mineral Laboratory in Guangzhou. The isotopic compositions were measured through CO_2 which is liberated from the reaction of carbonate and phosphoric acid. The evolved CO_2 gas is then conducted to and analyzed by Thermo-Finnigan GasBench coupled to Thermo-Finnigan MAT Delta Plus XP Continuous-Flow Isotope-Ratio Mass Spectrometer (CF-IRMS). The instrument was calibrated using $CaCO_3$ minerals by international isotopic standards NBS18 and NBS19. The testing values $\delta^{13}C$ and $\delta^{18}O$ are reported using the delta (δ) notation in permil (‰), relative to Vienna Pee Dee Belemnite (VPDB) for C and Vienna Standard Mean Ocean Water (VSMOW) for O, respectively, with precisions of 0.1‰ for C and 0.5‰ for O.

The measurement of trace element concentrations in pyrite was performed by LA-ICP-MS (Analytikjena PlasmaQuant MS Elite equipped with ESI NWR 193 nm excimer laser ablation system) at Beijing Createch Testing International Co. Ltd (Beijing). The laser beam was 30 μm in diameter and the ablation frequency was 6 Hz. Helium was applied as a carrier gas. The instrument was calibrated using NIST610 (Pearce et al., 1997) to make it stay in the optimal state. The sulfide external standard Mass-1 (called PS-1 in Wilson et al., 2002) and Fe content as the internal standard were used as reference material for trace elements measurement for this experiment. Data calibration depended on program GLITTER (ver. 4.4.4, Macquarie University) off-line (Griffin, 2008).

In-situ Sulfur isotope analysis was performed by using a Nu 1700 MC-ICP-MS system, equipped with sixteen Faraday cups and three ion counters at the State Key Laboratory of Continental Dynamics in Northwest University, Xi'an, China. The spot size was about 35 μm in diameter. The mass separation was calculated as 0.3333 in the analyses. The data were integrated as $^{32}S/^{34}S$ ($\delta^{34}S$ in ‰) ratio and normalized to Vienna-Canyon Diablo Troilite (V-CDT). Detailed descriptions of the measuring procedures are elaborated in Bao et al. (2017) and Chen et al. (2014).

Table 1
Rock information, γ, $\delta^{13}C$ and $\delta^{18}O$ of calcite cement, and temperature calculated by oxygen isotope data for the samples from the Beisantai deposit (Depth in m; $\delta^{13}C$ in ‰ and V-PDB; $\delta^{18}O$ in ‰ and V-SMOW; γ in nc/(kg·h); T in ℃; -, no measurement).

sample	depth	lithology	γ	$\delta^{13}C$	$\delta^{18}O$	T
19ZS01-1	934.12	Bluish-gray fine conglomerate	10	−29.2	20.3	14.02
19ZS01-2	933.83	Bluish-gray fine conglomerate	10	–22.8	21.1	10.77
19ZS01-3	933.68	Bluish-gray matrix-rich conglomerate at the interface between the bottom conglomerate and the overlying mudstone	22	–	–	–
19ZS01-4	932.93	Bluish-gray mudstone	11	–	–	–
19ZS01-5	932.13	Bluish-gray medium-course sandstone	10	−26.7	19.57	17.09
19ZS01-6	932.48	Bluish-gray pebbly sandstone	10	–23.9	20.3	14.02
19ZS01-7	927.76	Brownish-yellow pebbly sandstone	3	−6.52	17.62	25.80
19ZS01-8	925.73	Brownish-yellow fine conglomerate	5	−21.6	20.9	11.57
19ZS01-9	924.05	Brownish-yellow pebbly sandstone	3	−13.64	19.26	18.42
19ZS01-10	936.68	Green siltstone	4	−8.76	22.5	5.35
19ZS01-11	941.33	Green fine sandstone	3	−12.44	20.3	14.02
19ZS01-12	921.75	The interface between conglomerate and fine sandstone	11	−16.81	19.24	18.50
19ZS01-13	916.13	Green mud stone	3	–	–	–
19ZS01-14	834	Red mudstone	–	–	–	–
19ZS01-15	835	Red mudstone	–	–	–	–

4. Results

4.1. Lithologies and mineral assemblages

Mineralogical compositions of the bottom bluish-gray conglomerates and the middle brownish-yellow conglomerates were comparatively studied. Generally, they are consistent in the detrital grains that are mostly composed of fine-grained lithic fragments (Fig. 3A; mainly clastic rocks and some metamorphic, granitic, and volcanic rocks). Detrital minerals are mainly quartz and a small number of feldspar grains. Detrital accessory minerals such as zircon, apatite, magnetite, ilmenite, and monazite are occasionally observed.

The authigenic minerals show different assemblages in two zones. The bluish-gray conglomerates at the bottom part, with little interstitial matrix, are massively cemented by carbonate (20 ~ 40%), dominantly microcrystalline calcite followed by minor sparry calcite (Fig. 3A, B). Detrital grains are floating in the cement, suggesting that the rock was cemented at the early diagenetic stage. Many contemporaneous pyrites are enveloped in calcite cement (Fig. 3B), indicating a relatively reducing environment. Uranium minerals appear in the top margin of that conglomerate layer, which is characterized as a matrix-rich conglomerate, adjacent to an overlaid thin layer of mudstone (Fig. 2). For the ore-bearing rock (sample 19ZS01–3), the intergranular space is filled with abundant matrix micro-particles dominantly as quartz and

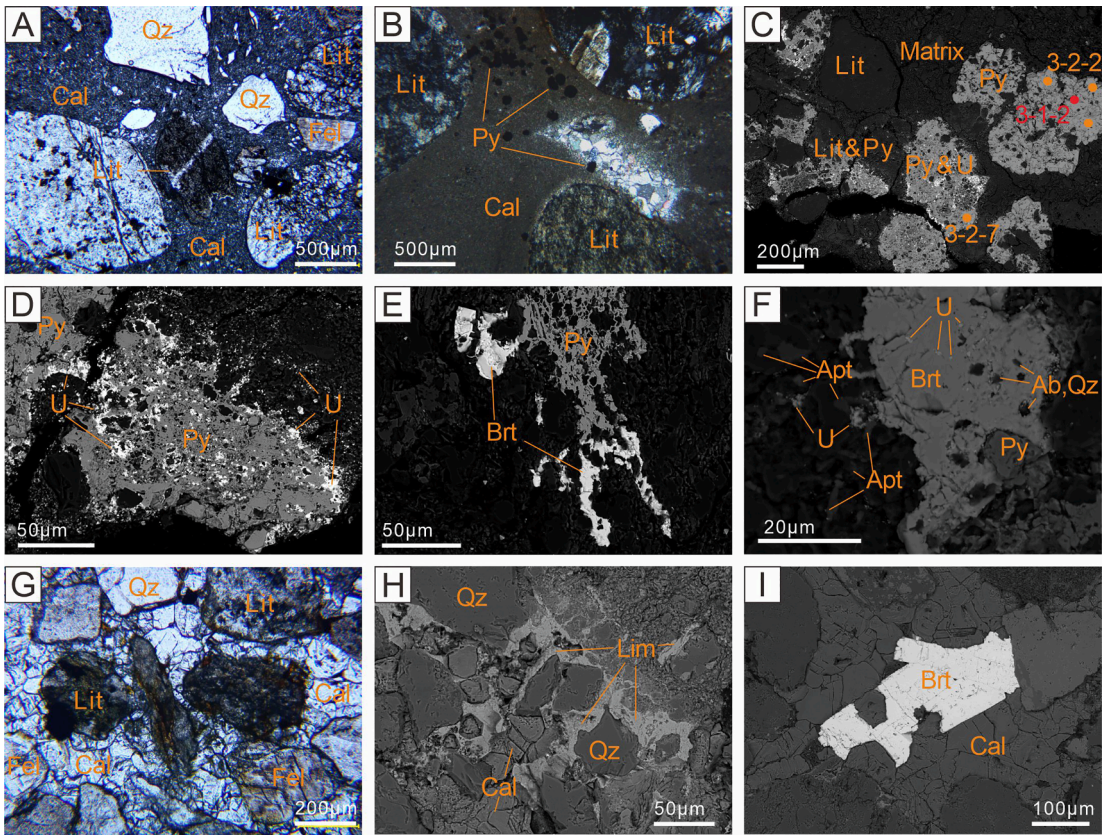


Fig. 3. Lithological characteristics of the samples from the bluish-gray zone (A-F) and the brownish-yellow zone (G-F). (A) The texture of conglomerate, showing pebbles floating in microcrystalline calcite cement. (B) The detritus are largely cemented by microcrystalline calcite and minor by sparry calcite, with some pyrites enveloped in it. (C) In the ore-bearing rock, pyrites and uranium minerals occur in the matrix conglomerate. (D) Ore-related pyrite, which is partly corroded and replaced by uranium minerals. (E) Barite partly replaces the edge of pyrite. (F) Pyrite and uranium minerals in barite. (G) The texture of conglomerate, cemented by sparry calcite. (H) Particles are cemented by calcite and limonite. (I) Barite and sparry calcite in the brownish-yellow zone. Fel-feldspar; Py-pyrite; Lit-lithic fragment; Qz-quartz; Brt-barite; Lim-limonite; Cal-calcite; U-uranium minerals. Orange circles indicate the location of spots for trace element analyses and red circles correspond to spots for sulfur isotopes measurements. (For interpretation of the references to color in this figure legend, the reader is referred to the web version of this article.)

feldspar as well as less biotite debris (Fig. 3C). The pores are also partly cemented by a small proportion of calcite. This ore-bearing rock carries the highest concentration of pyrite, which extensively occurs either in the intergranular space or pores and cracks in detritus (Fig. 3C). Uranium minerals are spatially related to certain pyrites that display common phenomenon of partial dissolution (Fig. 3D), suggesting that the uranium minerals should postdate the counterpart pyrites. Finally, some barites also occur in the ore-bearing rock in replacement pyrite (Fig. 3E), with residual uranium minerals and pyrites wrapped in it (Fig. 3F). Thus, barite is considered to be formed after uranium mineralization.

In the brownish-yellow zone, conglomerates are composed of more proportions of detrital grains with smaller sizes in diameter. Some particles show tangential intergranular contact (Fig. 3G). Likewise, rare interstitial matrix distributes in pores, where are mostly cemented by starry calcite (10 ~ 20%; Fig. 3G). Pyrite has been altered into barite and limonite (Fig. 3H, I), which causes the brownish-yellow in color of this zone. Some bluish-gray lenticles, incompletely oxidized remnants, can also be observed wrapped in the brownish-yellow rocks. Overall, sparry calcite, limonite, and barite represent the post-ore stage authigenic minerals.

Under BSE observation, the emplacement of uranium minerals is intimately related to the strong alteration in pyrite, calcite, matrix, and detritus (Fig. 4). Intensive alteration and associated mineralization in the matrix are generally centered on ore-related pyrite and the degree gradually decreases with distance (Fig. 5A). Unstable minerals such as feldspar and biotite in the matrix or detritus are readily to be dissolved and altered into clay minerals (Fig. 5B). The calcite cement has also undergone a certain dissolution, with lots of microcavities and cracks observed (Fig. 5C). Ore-stage alteration results in lots of secondary pores, which are beneficial for fluid migration and uranium adsorption (Fig. 5D). Except for the substitution of dissolved pyrite, uranium minerals are pervasively adsorbed on these secondary pores (Fig. 5D) and clay minerals (Fig. 5E).

4.2. Organic matter

The sediments are considered to be deposited under a weakly reducing environment for the green in color of the primary impermeable mudstones and siltstones. There is no organic matter such as black phytoclast or coal fragment macroscopically observed in hand specimen, except for one single micro carbonaceous debris found under SEM (Fig. 5F), which shows no spatial relationship with pyrites or uranium minerals.

To further characterize the typology of the organic matter in the sediments accurately, rock–eval pyrolysis was applied on samples, mainly mudstones that could have more content, from the bluish-gray zone and the green zone (Table 2). Total organic carbon (TOC) content of all the sampled organic matter is very low, ranging from 0.05 to 0.26%. In the green sandstone (sample 19ZS01–11) TOC value is extremely low, 0.05%, indicating that organic matter is rarely preserved. Rock-eval pyrolysis of free hydrocarbon (HC) in the samples reveals a very low content of thermodesorbed HC with S1 values of 0.07

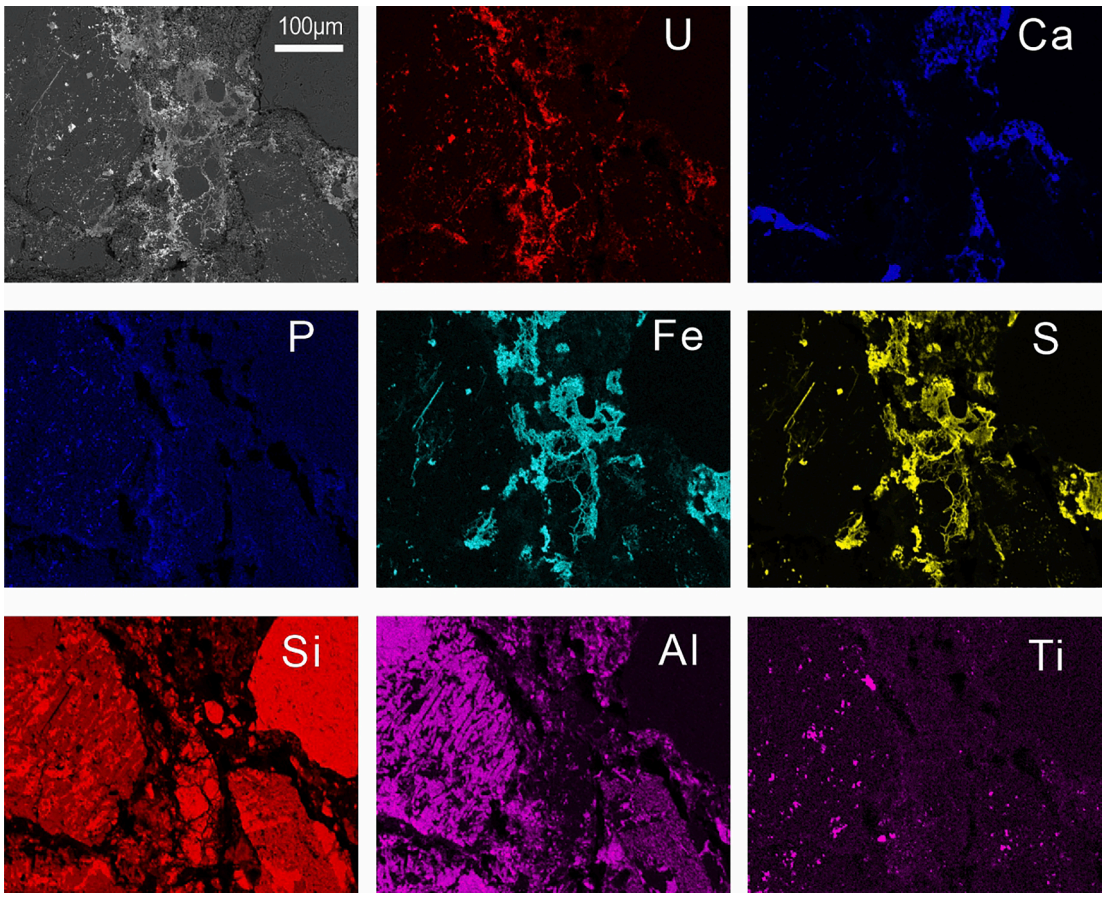


Fig. 4. Spatial relationship and mineral chemical information of pyrite and uranium minerals, with the EDS area scans of relevant elements (U, Ca, P, Fe, S, Si, Al, and Ti).

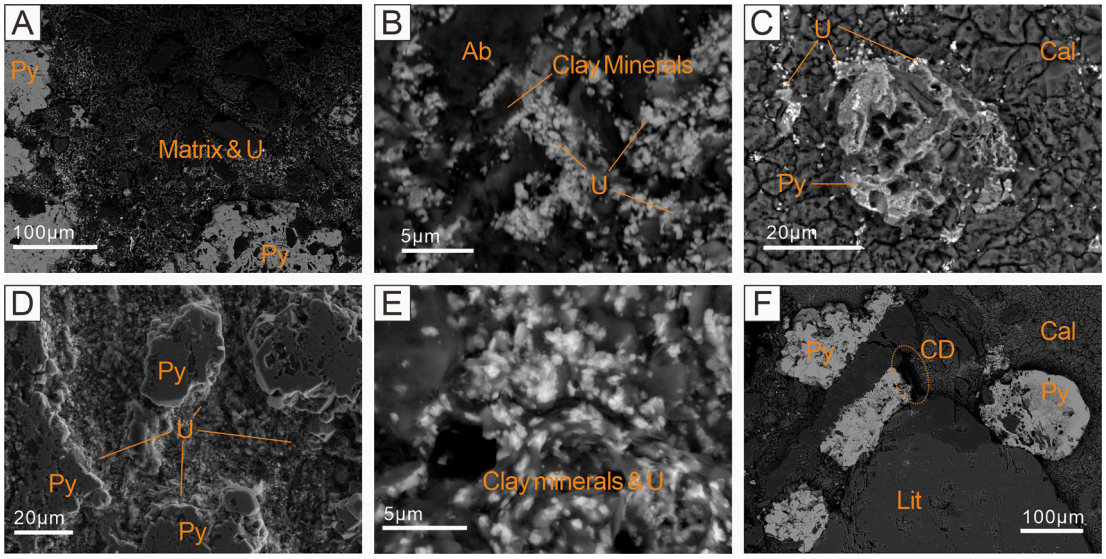


Fig.5. Microscopic characteristics of minerals. (A) Uranium minerals distribute in the matrix on the periphery of pyrite. (B) Uranium minerals and pyrites occur in the fine sandstone fragment in which unstable minerals are altered. (C) Microcrystalline calcite cement with lots of holes and cracks. One honeycomb-like pyrite locates in the center. (D) In an ore-bearing detritus, unstable minerals have been dissolved, resulting in secondary pores as the passageway for fluids and adsorption space for uranium minerals (SE image). (E) Uranium minerals intergrowth with clay minerals. (F) Carbonaceous debris in the ore-bearing rock. Py-pyrite; Lit-lithic fragment; U-uranium minerals; Cal-calcite; CD-carbonaceous debris.

to 0.21 mg HC/g sample. Rock-eval pyrolysis S2 data are also quite low, ranging from 0.2 to 0.35 HC/g sample, and indicate low petroleum potential (Espitalié et al., 1985). Except for sample 19ZS01–11, organic matter has a very low hydrogen index (HI), ranging from 96 to 167 mg HC/g TOC, and very low Oxygen index (OI) from 20 to 52 mg CO_2/g TOC. T_{max} values are lower than 435 ℃ and characterize thermally

Table 2
Rock-Eval Pyrolysis (REP) Results from samples of the Beisantai deposit (using REP interpretation methods of Espitalié et al., 1985).

Sample no.	lithology	TOC(%)	S1 (mg HC/g sample)	S2 (mg HC/g sample)	S3 (mg CO_2/g sample)	T_{max} (°C)	HI (mg HC/g TOC)	OI (mg CO_2/g TOC)
19ZS01-3	mudstone	0.21	0.17	0.35	0.05	351	167	52
19ZS01-4	mudstone	0.18	0.16	0.29	0.01	346	161	39
19ZS01-10	mudstone	0.26	0.14	0.25	0.05	343	96	31
19ZS01-11	sandstone	0.05	0.07	0.16	0.03	345	320	20
19ZS01-12	mudstone	0.11	0.07	0.1	0.03	338	91	36
19ZS01-13	mudstone	0.21	0.21	0.35	0.06	338	167	52

immature organic matter (Espitalié et al., 1985). These data indicate that the kerogen composition corresponds to type III or type IV (Fig. 6; Demaison et al., 1983) inherited from land plants. Given this, the indigenous organic matter can hardly create enough reducing agent for the reservoir conglomerates, where certainly have much lower content. There should be an external reductant supply for the Beisantai deposit.

4.3. C-O isotopes of calcite cement

For the broad calcite cementation, ten samples from different zones have been selected for the measurement of carbon and oxygen isotopic compositions (Table. 1; Fig. 7). The $\delta^{13}C_{PDB}$ values range from −29.2‰ to −6.52‰, displaying mixed sources. The samples from the bluish-gray zone show very low values (-29.2‰ ~ −16.81‰). The green zone calcite has a higher $\delta^{13}C$ signature (-12.44‰ ~ −8.76‰). The $\delta^{13}C$ values of brownish-yellow rocks range from −21.6‰ to −6.52‰. The oxygen isotopes vary in a narrow range that $\delta^{18}O_{V\text{-}SMOW}$ ranges from 17.62‰ to 22.5‰.

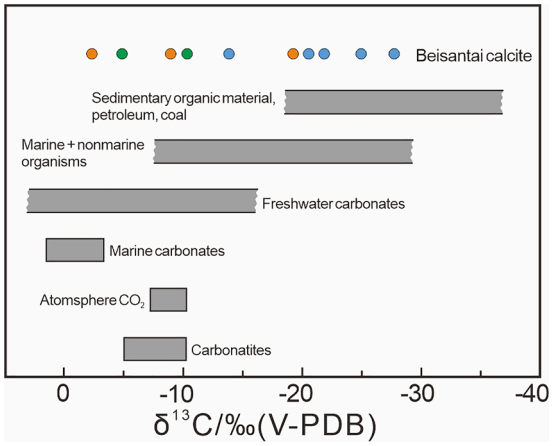


Fig. 7. Calcite $\delta^{13}C$ values of samples from different zones of the Beisantai deposit, indicating two main origins from freshwater and organic matter. $\delta^{13}C$ of various geological reservoirs were modified from Hoefs, (2015).

4.4. Pyrites

4.4.1. Morphology and texture

Pyrites are highly enriched in the bottom bluish-gray conglomerates, especially in the ore-bearing rock of the deposit. They mainly occur as (1) framboidal pyrite or euhedral crystals, cubic or polyhedral, with very small grain sizes (Fig. 8A), (2) sub-idiomorphic to idiomorphic grains or cement (Fig. 8B-D), with large sizes, (3) vine- or net-like pyrites, filling the fissures of detrital grains (dominantly in lithic siltstone) or in the matrix (Fig. 8E). Some of these pyrites intergrowth with uranium minerals are partially dissolved and replaced, which mainly occur as: (1) the edge of large pyrite is dissolved into irregular shapes as sawtooth or embayment and substituted by uranium minerals (Fig. 8F, G); (2) vine-like pyrites are partially cut and replaced by uranium minerals, with some incompletely dissolved pieces remained in it (Fig. 8D, H); (3) pyrite particles are enveloped by colloidal uranium minerals, in which the pyrites are corroded into anhedral (Fig. 8I); (4) the etched pits of pyrite are filled by uranium minerals (Fig. 8J-L).

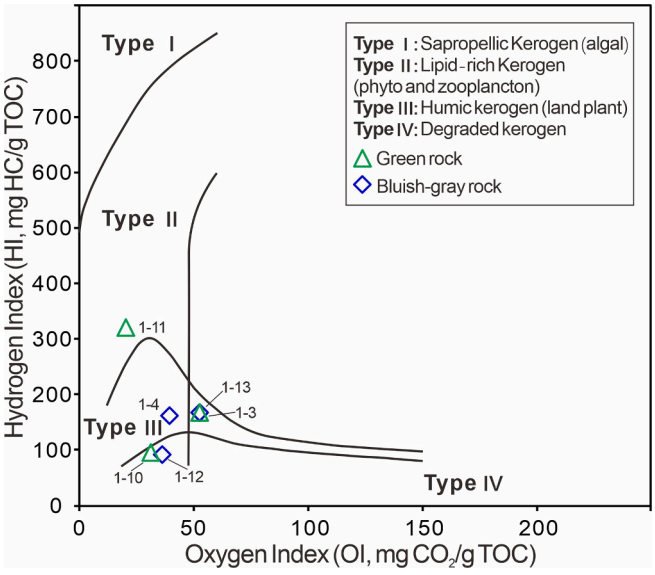


Fig. 6. HI v. OI diagram showing the typology of organic matter occurring in the samples of the Beisantai deposit (modified after (Herbin and Deroo, 1979; Demaison et al., 1983).

For further comparative study, the pyrites in the ore-bearing rock were subdivided into two groups according to their spatial relationship with uranium minerals (Table 3). Under the SEM observation, individual pyrites have relatively larger particle sizes, better perfection, and weak alteration (Fig. 8B, C). In contrast, ore-related pyrites show more complicated morphology with stronger corrosion (Fig. 8D-L). It is worth mentioning that some pyrites show distinctive biotic oxidation textures as numbers of oriented deep corrosion pits or honeycomb-like structures (Fig. 9A-C) different from cracks or shallower pits caused by chemical dissolution.

4.4.2. Trace elements characteristics of pyrite

The trace element concentrations of pyrite, both the individual ones and ore-related ones occurring in the ore-bearing rock, were measured by LA-ICP-MS. Both the two groups have similar patterns of higher Mn, Mo, Zn concentrations, and minor Cu, V, and Sb content (Fig. 10, Table 4). Whereas, there is a progressive decrease of As, Se, and especially Ni and Co concentrations from individual to ore-related pyrites (Fig. 10; Fig. 11A, B). The individual pyrites have higher As (91.68 ~ 836.68 ppm; median = 236.055 ppm), Se (50.37 ~ 2404.12 ppm; median = 318.635 ppm), Ni (12.09 ~ 395.51 ppm; median = 84.795 ppm), and Co (9.74 ~ 442.14 ppm; median = 83.135 ppm) contents. Ore-related ones are characterized by lower As (26.81 ~ 213.24 ppm; median = 110.61 ppm), Se (36.22 ~ 162.13 ppm; median = 125.815 ppm), Ni (3.34 ~ 48.11 ppm; median = 10.355 ppm), and Co (0.851 ~ 16.91 ppm; median = 7.22 ppm) contents.

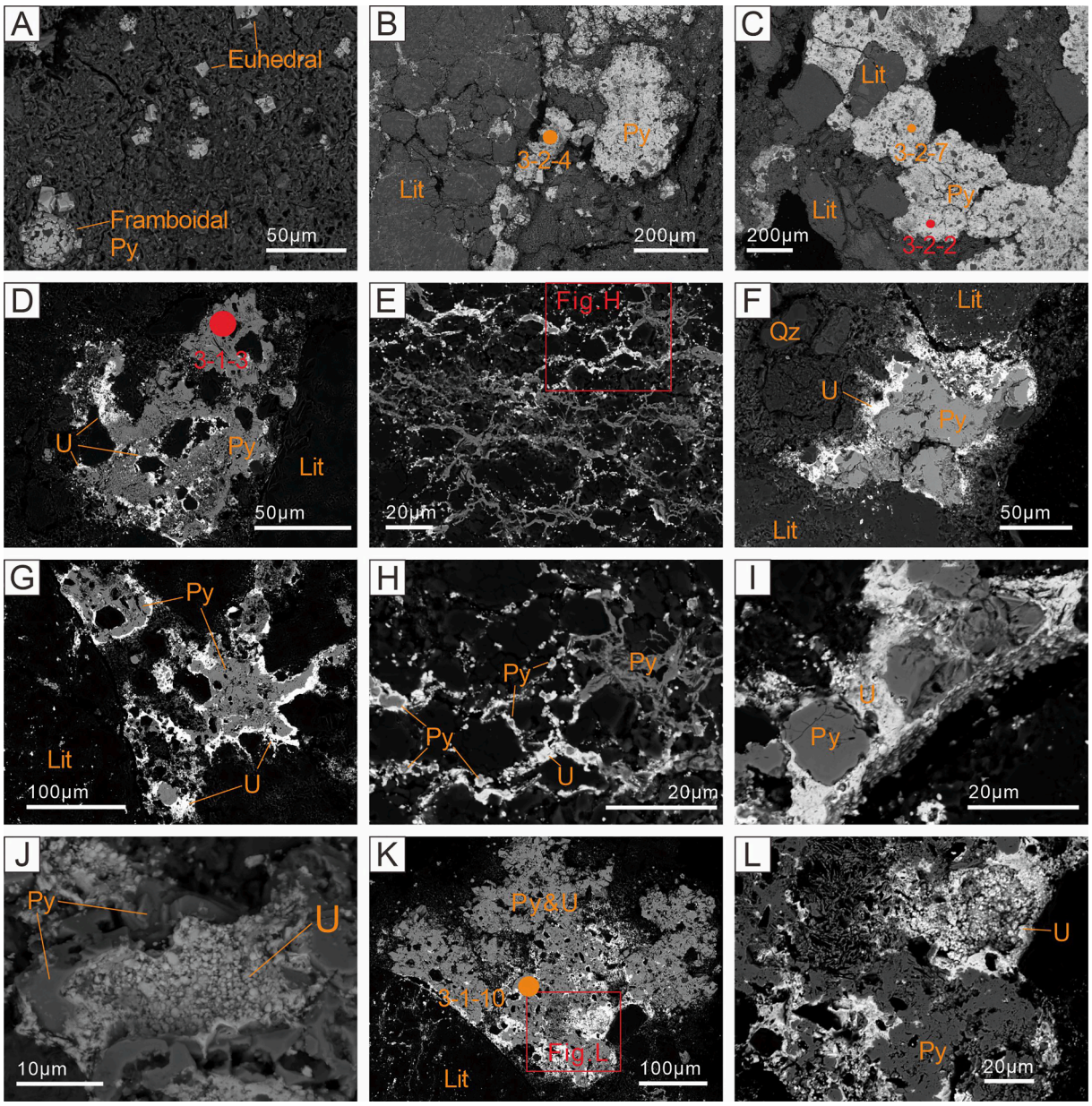


Fig. 8. Uranium minerals in replacement of pyrites. (A) Framboidal pyrite and euhedral pyrite. (B-C) Individual sub-idiomorphic pyrite. (D) Ore-related pyrite, which is partly corroded and replaced by uranium minerals. (E) vine-like pyrites and uranium minerals in fissures of lithic siltstone. (F-G) Pyrites are partly dissolved and replaced by uranium minerals. (H) Enlargement of the rectangle in (E) showing the vine-like pyrites are partially replaced by uranium minerals. (I) Colloidal uranium minerals envelope small pyrite crystals. (J-K) Globular cocci-shaped uranium minerals fill in etched pits of pyrite. (L) Enlargement of the rectangle in (K). Py-pyrite; Lit-lithic fragment; Qz-quartz; U-uranium minerals; Cal-calcite; Orange circles indicate the location of spots for trace element analyses and red circles correspond to spots for sulfur isotopes measurements. (For interpretation of the references to color in this figure legend, the reader is referred to the web version of this article.)

4.4.3. *Sulfur isotope signature*

Pyrites in the ore-bearing rock were analyzed to reveal the origin. The results of the pyritic $\delta^{34}S$ show extremely negative values within a narrow range, between −48.38‰ and −35.65‰ (Table 5; Fig. 12), in which the $\delta^{34}S$ values of pyrite related to U minerals (n = 6) ranging from −41.29‰ to −35.65‰ (mean = -39.46‰); the individual pyrites (n = 5) have a slightly lower signature from −48.38‰ to −41.12‰ (mean = -43.71‰). These representative isotopic signatures likely indicate the important role of SRB during pyritization.

4.5. *U minerals*

By way of SEM observation, all the uranium minerals occur as coffinite, containing high U, O, and Si and less P and Ca identified by EDS (Fig. 9D). Coffinite mainly occurs as monocrystal, aggregate (Fig. 5B), or colloidal form (Fig. 8I). They consist of microspheric nanocrystals, generally smaller than 1 μm, exhibiting coccoid morphology. These minerals are closely associated with strongly dissolved pyrites as stated above, surrounding the pyrites or disseminated in the corroded matrix or detritus on the periphery of the ore-related pyrites (Fig. 4).

Table 3
Characteristics of individual pyrite and ore-related pyrite in the ore-bearing rock of the Beisantai deposit.

Characteristics	Individual pyrite	Pyrite intergrowth with coffinite
Particle size	Mostly between 100 μm and 500 μm; some larger than 500 μm.	Mostly smaller than 300 μm; little between 300 and 500 μm.
Distribution pattern	Mostly occurring in the large intergranular spaces.	Mostly occurring in the narrow intergranular spaces or in fissures and pores of detritus.
Morphology	Sub-idiomorphic to idiomorphic. The shape is barely restricted by detritus. The edges are usually end up with smaller euhedral crystals.	Sub-idiomorphic to xenomorphic. The shape is usually restricted by detritus. Some of the edges are irregular due to dissolution.
Corrosionfeatures	Light corrosion or no corrosion.	Moderate to severe corrosion.

5. Discussion

5.1. Stable isotopes of calcite cement and implications for fluids

5.1.1. Oxygen isotopes

In order to better understand the depositional environment of calcite cement, it is necessary to constrain the temperature during calcite cementation. Oxygen isotope fractionation between parental water and calcite is greatly affected by temperature, so oxygen isotopic signature can approximately reveal the fluid property as a geological thermometer. The oxygen isotopic compositions of different zones have a narrow range, from 17.62‰ to 22.5‰, and mainly concentrate between 19.24‰ and 21.1‰ (Table. 1). The calcite formation temperature was calculated using the equation proposed by Friedman and O'Neil (1977):

$$1000ln\alpha_{calcite-water} = 2.78 \times 10^6 T^{-2}(K) - 2.89 \quad (1)$$

Since there is no magmatic and corresponding hydrothermal activity recorded in Cenozoic in the study area, we adopt modern shallow groundwater in east Junggar Basin (mean $\delta^{18}O_{V\text{-}SMOW} = -10.9‰$; Li et al., 2015) as parental fluid isotopic composition during calcite precipitation, assuming a similar condition from the Neogene to the present. The outcomes listed in Table 1 demonstrate that the temperature of parental fluid of the calcite cement is very low, ranging from 5.35 ℃ to 25.8 ℃ (mean T = 14.96 ℃). Although these values could not represent the real paleo-temperature in the reservoir, it approves the low-temperature supergene environment during the calcite cementation. This is consistent with the observation of lacking quartz overgrowth and the bare occurrence of fluid inclusions in calcite cement. During the Cenozoic, the Shawan Formation has been continuously subsiding (Liao et al., 2002) and is currently at its maximum depth. Previous studies have obtained that the present temperature of the Neogene Shawan Formation is approximately 40℃, at the depth of ~ 950 m at a geothermal gradient of 24.2 ℃/km (Wang and Chen, 1990), which is in accordance with the burial-thermal history of the Beisantai Swell (Liao et al., 2002; Zhang et al., 2018; Liu et al., 2020a; Liu et al., 2020b). This can be regarded as the upper temperature limit of the

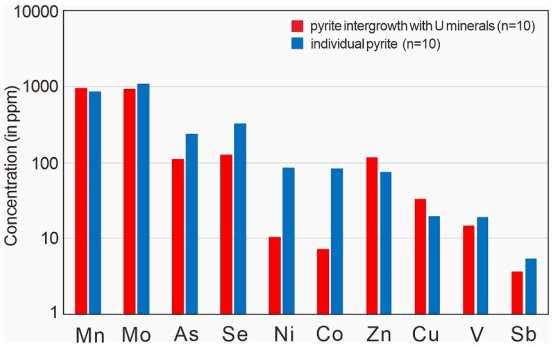


Fig. 10. Trace element concentrations of pyrite occurring in the ore-bearing rock, which was subdivided into two groups according to whether intergrown with uranium minerals. Median values are presented in the diagram.

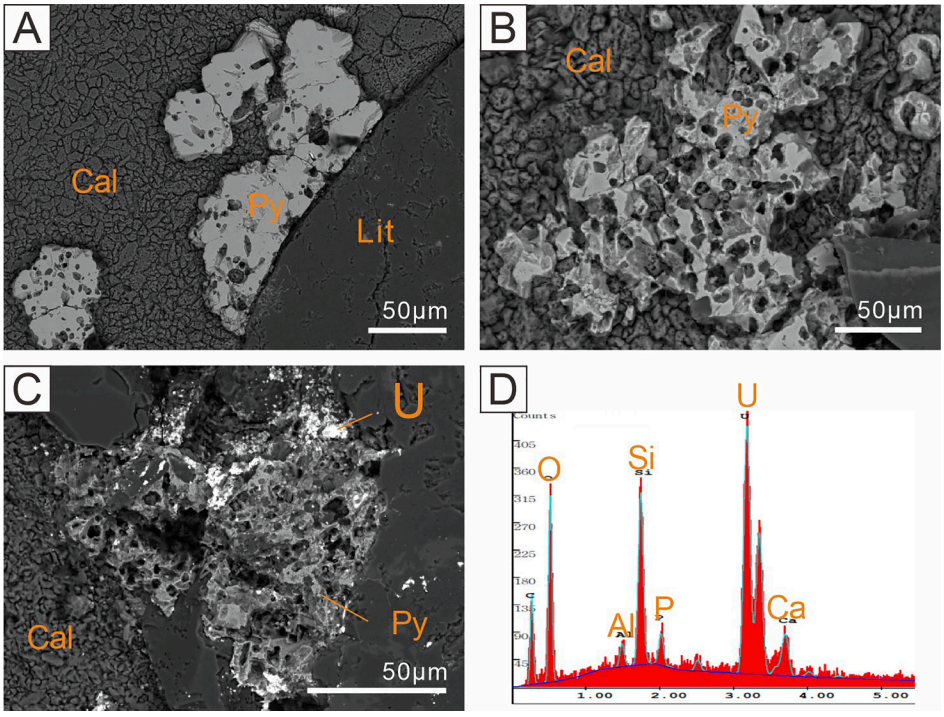


Fig. 9. (A-C) Microscopic characteristics of the bio-oxidation of pyrite. (D) EDS Spectrum for uranium minerals in the Beisantai deposit. Py-pyrite; U-uranium minerals; Cal-calcite; Lit-lithic fragment.

Table 4
Representative trace element concentrations of two groups of pyrite occurring in the ore-bearing rock of the Beisantai deposit.

Group	ore-related pyrite									
Anlysis no.	3–1-1	3–1-2	3–1-3	3–1-4	3–1-5	3–1-6	3–1-7	3–1-8	3–1-9	3–1-10
V51	4	22.3	22.56	9.52	18.35	6.92	30.22	10.68	<0.73	<0.69
Mn55	707.26	929.76	1023.37	798.34	942.5	921.6	910.11	1009.34	1473.61	1714.6
Co59	0.851	11.24	3.86	2.29	3.09	15.31	16.91	8.7	10.68	5.74
Ni60	3.43	18.33	10.7	8.77	7.9	48.11	24.81	10.01	12.88	9.22
Cu65	2.6	33.34	44.81	23.28	36.51	88.41	95.04	32.23	21.38	20.33
Zn66	16.5	67.97	145.8	231.37	136.99	966.69	147.72	53.93	97.09	68.44
Ga71	0.304	2.29	3.07	0.59	2.44	0.913	5.04	1.219	10.95	3.53
Ge72	5.33	5.56	6.62	4.68	6.29	4.76	5.83	5.46	12.65	5.82
As75	26.81	143.11	99.32	110.1	93.85	213.24	150.7	90.17	156.02	111.12
Se77	36.22	131.38	125.1	51.77	99.53	162.13	137.42	100.29	126.53	136.83
Mo95	434.71	1046.48	855.09	575.12	955.08	894.94	960.68	640.99	1706.24	1288.98
Group	Individual pyrite									
Anlysis no.	3-1-11	3-1-12	3-2-1	3-2-2	3-2-3	3-2-4	3-2-5	3-2-6	3-2-7	3-2-8
V51	17.82	<0.62	10.97	36.73	11.63	<2.13	53.36	19.73	7.65	26.03
Mn55	762.79	185.55	980.4	180.64	842.98	927.74	878.53	1127.74	917.24	425.13
Co59	9.74	25.96	115.22	151.62	149.93	24.41	442.14	41.61	84.02	82.25
Ni60	12.09	17.94	106.17	135.71	142.05	72.56	395.51	30.75	44.56	97.03
Cu65	4.55	15.09	16.02	247.39	3.53	132.83	27.73	22.63	6.57	29.12
Zn66	73.86	94.2	56.54	91.48	71.01	191.67	153.41	60.75	34.2	72.99
Ga71	1.439	3.67	2.45	2.56	1.432	8.15	3.64	1.718	0.716	2.87
Ge72	4.39	4.95	4.35	4.89	4.55	6.03	4.55	4.8	4.29	4.76
As75	100.35	199.85	91.68	836.68	505.16	272.26	735.04	170.69	144.63	367.92
Se77	69.58	50.37	379.81	257.46	2404.12	107.7	2003.23	589.5	619.33	135.82
Mo95	737.94	1313.52	1985.92	677.32	840.87	1888.42	1424.25	1546.03	568.38	718.35

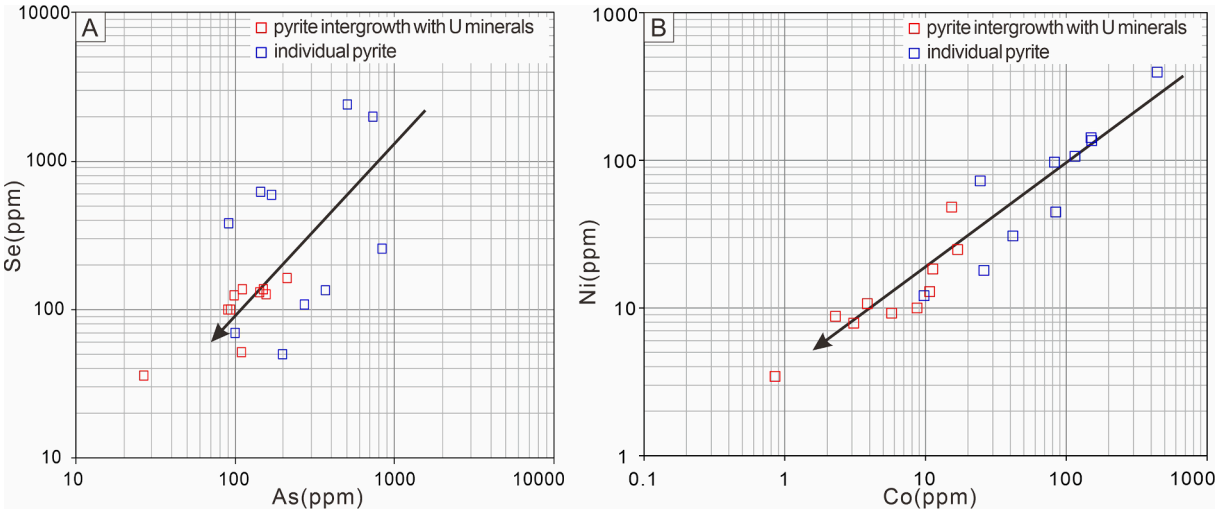


Fig. 11. As vs. Se (A) and Co vs. Ni (B) diagrams showing the trace element concentrations decrease from individual pyrite to ore-related pyrite. The plot demonstrates how pyrites formed at the early stage appear consistently more enriched in As, Se, Co, and Ni than pyrites formed at the late stage.

Table 5
In-situ sulfur isotopic analysis of representative pyrite in the ore-bearing rock.

Groups	Analysis no.	$\delta^{34}S_{V\text{-}CDT}$ (‰)	2SE
Ore-related pyrite	3–1-1	−35.5649	0.206264
	3–1-2	−41.2887	0.24526
	3–1-3	−40.261	0.24249
	3–1-4	−40.678	0.233265
	3–1-5	−40.3399	0.530003
	3–1-6	−38.6466	0.3094
Individual pyrite	3–1-7	−48.3849	0.197539
	3–1-8	−43.7287	0.372305
	3–2-1	−42.8369	0.422978
	3–2-2	−42.4926	0.154682
	3–2-3	−41.1204	0.252058

Beisantai deposit. Besides, the low homogenization temperatures of oil and gas inclusions from the deep Permian to Jurassic reservoirs, with average temperatures ranges from 42.0 to 66.6 ℃ (Liao et al., 2002), suggest that this deduction is acceptable. Therefore, the oxygen fractionation temperature is considerable and it can be inferred that the interlayer alteration and cementation processes were occurred at a supergene low-temperature environment before the deep burial by overlying thick sediments.

5.1.2. *Carbon isotopes*

Generally, carbonate cement has serval potential carbon sources, including (1) endogenetic sources, e.g., magmatism, (2) carbon dioxide (CO_2) in atmosphere, (3) carbonates and bicarbonates dissolution, and (4) organic matter oxidation (Zhao et al., 2018). The $\delta^{13}C$ values of carbonate cement have been used to identify the origin of carbon, for different reservoirs are usually characterized by certain ranges of isotopic compositions (Hoefs, 2015; Sharp, 2017). The diagenetic

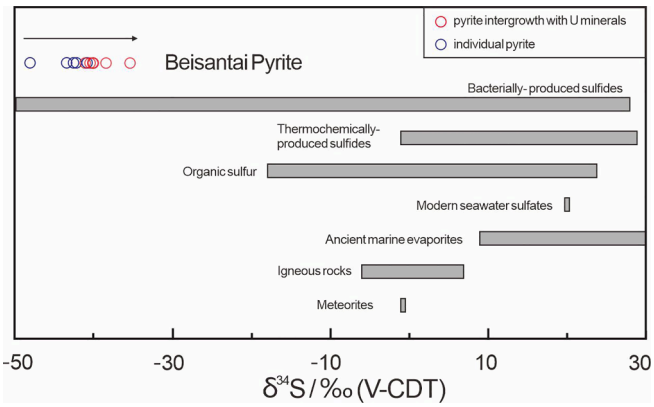


Fig. 12. Pyrite $\delta^{34}S$ indicating its origin of bacterial sulfate reduction. $\delta^{34}S$ geological reservoirs were modified from (Kaplan and Rittenberg, 1964; Aplin and Coleman, 1995; Seal, 2006; Hoefs, 2015).

microcrystalline calcite and the epigenetic sparry calcite occurring in different zones can reflect the properties of the formation fluid and the external fluid, respectively. Combined with the carbon isotopic signature of each zone, the origin and genesis of calcite cements can be determined.

The $\delta^{13}C$ values are broadly heterogeneous (Fig. 7). For the green zone, the $\delta^{13}C$ values, −12.44‰ ~ −8.76‰, reflect the predominance of fresh groundwater and atmospheric CO_2 origin. The siltstone and fine sandstone in the green zone are strictly restricted by thick aquicludes, thus these rocks can hardly be affected by external fluids. The bluish-gray conglomerates and sandstones are massively cemented by diagenetic microcrystalline calcite (Fig. 3A, B). The extremely low $\delta^{13}C$ values, as low as −29.2‰, reflect the tremendous contributions of organic carbon. Since the much higher $\delta^{13}C$ values in the primary green zone, indigenous organic matter could have very limited influence on calcite cementation. Moreover, indigenous organic matter content in the conglomerates should be much lower than the adjacent siltstones or mudstones which show very low contents (Table 2). The enhanced amount of syngeneic pyrites sealed in calcite (Fig. 3B) also indicate the injection of external reducing materials. Therefore, the organic carbon probably originated from extrinsic hydrocarbons such as the upward migrated oil and gas. Under SEM observation, there are extensive dissolution characteristics in microcrystalline calcite, resulting in numerous cracks and micro-cavities (Fig. 5C, 9A-C). This is likely to be caused by organic acids or excess CO_2 produced through the biodegradation of organic matter at the late stage (Edman and Surdam, 1986). Therefore, the formation fluid in the bluish-gray rocks can be characterized as acidic and reductive.

The permeable layer has also been subjected to epigenetic alteration and metasomatism to varying degrees by the infiltrated interlayer fluid, resulting in uneven increases in the proportion of sparry calcite (Fig. 3G, I) and heavy carbon isotope. This is liable to the increase of $\delta^{13}C$ value in the bluish-gray zone, up to −16.81‰ (sample 19ZS01-12). The broad $\delta^{13}C$ values of brownish-yellow rocks indicate that the carbon sources are the mixture of organic carbon and external heavier carbon carried by infiltrated groundwater. The lowest value of −21.6‰ represents a higher proportion of organic carbon remained after weaker alteration. This is in accordance with the bluish-gray lenticles that remained in the yellow zone. The higher values, −13.64‰ ~ −6.52‰, are corresponding to freshwater and atmospheric CO_2 origin. In any case, it can be confirmed that the infiltrated interlayer fluid is alkaline with appreciable carbonate dissolved.

5.2. Biogenic origin of pyrite and constraint on uranium mineralization

5.2.1. Bacterial sulfate reduction originated pyrite

Pyrites in the ore-bearing rock are characterized by a strong deficiency of ^{34}S (Table 5; Fig. 12), with $\delta^{34}S$ ranging from −48.38‰ to −35.65‰ (mean = -41.39‰). Such negative values are originated far from other ways but biogenic process, for they are much lower than the lightest value of organically derived sulfur approximately −17‰ (Aplin and Coleman, 1995; Cai et al., 2002). Bacteria are very active in supergene low-temperature condition (Knoblauch and Jorgensen, 1999; Moosa et al., 2005). Sulfite-reducing bacteria (SRB) are widely existed in the sedimentary strata and are identified to play a significant role in the formation of metal sulfide deposits (Min et al., 2005a, b; Cai et al., 2007a, b; Ingham et al., 2014; Bonnetti et al., 2015; Akhtar et al., 2017; Bonnetti et al., 2017; Zhao et al., 2018; Rallakis et al., 2019). Bacterial sulfate reduction (BSR) produces reduced species (H_2S (aq), HS^-; Machel, 2001) that are strongly depleted in ^{34}S (Habicht and Canfield, 1997; Brunner and Bernasconi, 2005), reacting with iron minerals (such as Fe oxides/hydroxides) to form pyrite (Botsou et al., 2015; Børresen, 2017). Moreover, the lower isotope value (-48.38‰) are supposed to be generated from multi-step reactions (Cai et al., 2007a; Ulrich et al., 2011) for it is hard to achieve such huge fractionation through single-step BSR, as performed on pure culture experiments (Kaplan and Rittenberg, 1964). Indeed, it is not uncommon in interlayer oxidation zones of formation for the persistent down dip transportation of redox front via multiple dissolution and re-precipitation of pyrite (Bonnetti et al., 2020).

5.2.2. The process of pyritization and the implications

Comparing the two groups of pyrites in the ore-bearing rock, though they both have the same origin, BSR, there are differences in occurrence and geochemical features. Most of the individual pyrites have much larger sizes and more idiomorphic crystal forms (Table 3). They are mostly emplaced with more capacious space during the diagenetic to the epigenetic stage that their morphologies are less restricted by detritus (Fig. 8B, C). Ore-related pyrites with smaller sizes are usually shaped by detrital grains, filling the narrow intergranular space or fissure of grains, resulting in complex morphologies that are also partly caused by the intensive corrosion (Fig. 8D-L).

In the pore systems of conglomerate, the space for fluid flow and mineral emplacement are controlled by diagenesis mainly through compaction and filling and cementation of authigenic minerals. During the gradual closure of pores, the early precipitated pyrites are supposed to obtain more and better space and material supply, including sulfur and reductant. Meanwhile, the pyritization also results in the sealing of the major fluid passageways. Afterwards, the interlayer fluid influx slows down and the paths transfer to the poor residual pores. The late pyrite precipitated in a lower porosity is characterized as smaller size as a result of the decreased supply of reduced sulfur. Besides, the positions where the late pyrites precipitate represent local open systems at that time, where provides ways for the interaction between the later ore-bearing fluid and materials in the formation. Therefore, the process of pyritization can be expressed as the gradual sealing of pores, which is accompanied by a decrease in the supply of organic matter, leading to the slowdown in the rate of BSR and pyrite precipitation.

This trend also corresponds to the changes in sulfur isotopes and trace elements between the two groups. Comparatively, slightly lighter signatures (mean $\delta^{34}S$ = -43.71‰) of the sulfur isotope are displayed among the individual pyrites than the ore-related pyrites (mean $\delta^{34}S$ = -39.46‰) (Fig. 12). Although the changes are small, it is likely to reflect the changes in compositions of fluid, which can be attributed to the quick consumption of ^{32}S in the early stage and the lower rate of BSR in the late stage, within a gradually closed system. Due to light sulfur isotope is superior to be utilized by SRB (Cai et al., 2007a, b), which can cause the decrease of ^{32}S available in solution with the continuous precipitation of pyrite. Although the pyritization was processed in an

open system, a series of factors including the decrease in the supply of ^{32}S, the decline of the SRB communities, and the accumulation of ^{34}S in the formation, could cause the slight increase in $\delta^{34}S$ values.

Likewise, there are considerable decreases in the content of the ore-related pyrite on Ni and Co as well as minor on As and Se. From the plots of Fig. 11, progressive decreases display from the individual pyrites, with higher values and broader variation ranges, relative to the ore-related ones, with low but concentrated values. As, Se, Ni, and Co are easily incorporated into pyrite during BSR (Teclu et al., 2008; Qian et al., 2013; Le Pape et al., 2017) under reducing conditions (Amrhein et al., 1993; Diehl et al., 2012; Kusebauch et al., 2018), for these elements play essential biochemical roles in their metabolic processes (Dungan and Frankenberger, 1999; Dopson et al., 2003; Barton et al., 2007). Concentrations of As and Se that are both greatly affected by reducibility and microbes show a slight decrease as the gradually weakened BSR. In the same way, Co and Ni contents that are less affected by redox potential have a sharp drop from the early stage to the late stage. This provides the same indication as to the sulfur isotopic signatures. In addition, trace elements such as Mn, Mo, Zn, Cu have similar patterns of contents, suggesting that the composition of parental fluid remained stable during the pyritization stage. Combined with their occurrence and the small changes in geochemical properties, a successive progress of pyritization in the ore-bearing rock can be revealed. The pyritization has lasted a relatively short period of time, in which the ore-related pyrites precipitate at the late stage. The occurrence of the abundant pyrites in the ore-bearing rock provides the significant material basis for the subsequent uranium mineralization.

5.2.3. Relationship between pyritization and uranium mineralization

Pyrite is one of the most common minerals associated with uranium, especially widely distributed in the oxidation–reduction transitional zone of sandstone-type deposits, and is generally considered as an indicator for redox environment (Cai et al., 2007a, b; Wignall et al., 2009; Ingham et al., 2014; Wei et al., 2016; Chen et al., 2019; Yue et al., 2019, 2020; Bonnetti et al., 2020). Studies about the genesis of BSR originated pyrite and the coexisted uranium minerals are mainly demonstrated as organic matter related reduction under low-temperature conditions (e.g., Rackley, 1972; Granger and Warren, 1974; Reynolds and Goldhaber, 1978), involving biogenic mechanisms for both sulfate reduction and uranium mineralization (Min et al., 2005a, b; Cai et al., 2007a, b; Bonnetti et al., 2015), with the contribution of sulfate-reducing bacteria (SRB; Southam and Saunders, 2005), which is able to utilize organic matter as nutrient reducing sulfates to sulfides simultaneously with reduction of U(VI) to insoluble U(IV) ore (Lovley et al., 1991; Lovley and Phillips, 1992; Spear et al., 1999; Sani et al., 2004; Cai et al., 2007a, b). SRB are approved capable of utilizing U(VI) as the preferred electron acceptor for respiration and reduced to U(IV) directly (Lovley et al., 1991; Lovley and Phillips, 1992; Sani et al., 2004; Spear et al., 1999). Light sulfur isotope is preferential for bacteria, hence these pyrites, characterized by strongly enriched in ^{32}S, are generally interpreted as resulting from BSR (Jensen, 1958; Belyi et al., 1972). This speculation is primarily based on the paragenetic relationship between uranium minerals and the intimate intergrown biogenic pyrites but without replacement, which suggests that they are precipitated either simultaneously or in succession within a short time. By the way, the enriched organic matter in these deposits provides a shield for pyrites and uranium ores, protecting them from dissolution or decomposition by post-ore stage fluids.

In the Beisantai deposit, the mineralization shows much difference to previous studies. Despite the abundant pyrites, the barely preserved organic matter and the widespread coffinite replacement of ore-related pyrite are the most notable features. Thus, it is necessary to discuss the relationship between the periods of pyritization and U mineralization, which is the key to investigate the relationship of pyrite and the uranium ore. As stated above, the dissolved ore-related pyrites are the late-stage ones; therefore, the scenario of the dissolution of early pyrites while the precipitation of new pyrites is unlikely to happen simultaneously during the ore stage. Uranium should precipitate during or after the large-scale dissolution of pyrites, when pyritization and BSR have ceased, resulted from the exhaustion of organic matter and the increase of redox potential (Fig. 13).

5.2.4. Pyrite dissolution contributions to uranium precipitation

The significant role of pyrite in sandstone-type uranium deposits has been investigated in previous studies, not only as adsorption sites for providing large surface (Goldhaber et al., 1987; Eglizaud et al., 2006; Qafoku et al., 2009; Miao et al., 2010) but also as one of the reductants resulting in the transformation of U(VI) to sparingly soluble U(IV) (e.g. Jensen, 1958; Granger and Warren, 1974; Leibold, 2013; Gallegos et al., 2015). The interaction of aqueous U(VI) with pyrite surface has been manifested depending on many experiments (Wersin et al., 1994; Eglizaud et al., 2006; Ma et al., 2020). It is also reported that pyrite can generate H_2S, which is a strong reductant, after reaction with water under an anoxic environment (Chen and Guo, 2007; and references therein).

Indeed, it is found that pyrite oxidation rates remain quite slow even under acidic conditions without being mediated by bacteria (Pisapia et al., 2007; Yin et al., 2020). Pyrite oxidation microorganisms such as *Acidithiobacillus thiooxidans* and *Acidithiobacillus ferrooxidans* (an iron- and sulfide-oxidizing bacterial species commonly present in natural environments) are known to increase oxidation and dissolution rates of pyrite greatly (Mustin et al., 1992; Sasaki et al., 1998; Boon et al., 1999; Toniazzo et al., 1999; Fowler et al., 2001; Yu et al., 2001; Jones et al., 2003; Pisapia et al., 2008). Uranium can be reduced mediated by either metabolically produced reducing compounds or directly use of U(VI) as a final electron acceptor (Gargarello et al., 2009, 2010; Zhang et al., 2020). Due to the efficient reaction rates, microbially mediated reduction of U(VI) to immobilized U(IV) minerals has been applied into the field of remediation of the environment from radioactive contamination (Wersin et al., 1994; Wu et al., 2006, 2007; Gargarello et al., 2009).

In the Beisantai deposit, distinct bio-oxidation features can be observed on pyrites. This is characterized by the perforative corrosion features, consisted of deep, geometric (squares, lozenges, pseudo-hexagons), and oriented holes in pyrite or honeycomb-like structures (Fig. 5C; 9A-C), distinguished from cracks or shallow tiny pits caused by abiotic oxidation. These phenomena seriously resemble the biotic controlled patterns described by Jiang (2006), Pisapia et al. (2008), Liu and Zhang (2011), and Jiang et al. (2011). Thus, there were drastic bacterial activities in the Beisantai deposit, which probably had been involved in the pyrite oxidation and uranium mineralization. The microbially mediated uranium mineralization can also be approved by the high content of phosphorus uranium minerals (Gächter and Meyer, 1993; Alessi et al., 2014) and the microbial-like textures, as globular cocci (Fig. 5B, 8 J, L) that is proposed to be evidence of biogenic origin (Min et al., 2005a, b; Cai et al., 2007a, b; Zhao et al., 2018). The tinny irregular apatite fragments scattered in the matrix (Fig. 3F) might be the remnants of bacterial metabolism (Hutchens et al., 2006; Feng et al., 2011). Therefore, all these aforementioned factors support the speculation of microbial-mediated uranium reduction based on pyrite.

5.3. Uranium mineralization

Uranium is sensitive to redox potential and its mineralization in supergene deposits has been generally attributed to U(VI) reduction by reductants (e.g. sulfides and organic matter) under low-temperature conditions (Rackley, 1972; Granger and Warren, 1974; Reynolds and Goldhaber, 1978). Coffinite is likely to precipitate from neural to weakly alkaline fluids, with high silicate concentrations (Mercadier et al., 2011; Szenknect et al., 2016). As is shown in Fig. 14, both the decrease of Eh and pH lead to coffinite precipitation (Cumberland et al., 2016). In general models for the interlayer oxidation-type uranium deposit, uranium is transported by oxidising groundwater to the redox front where

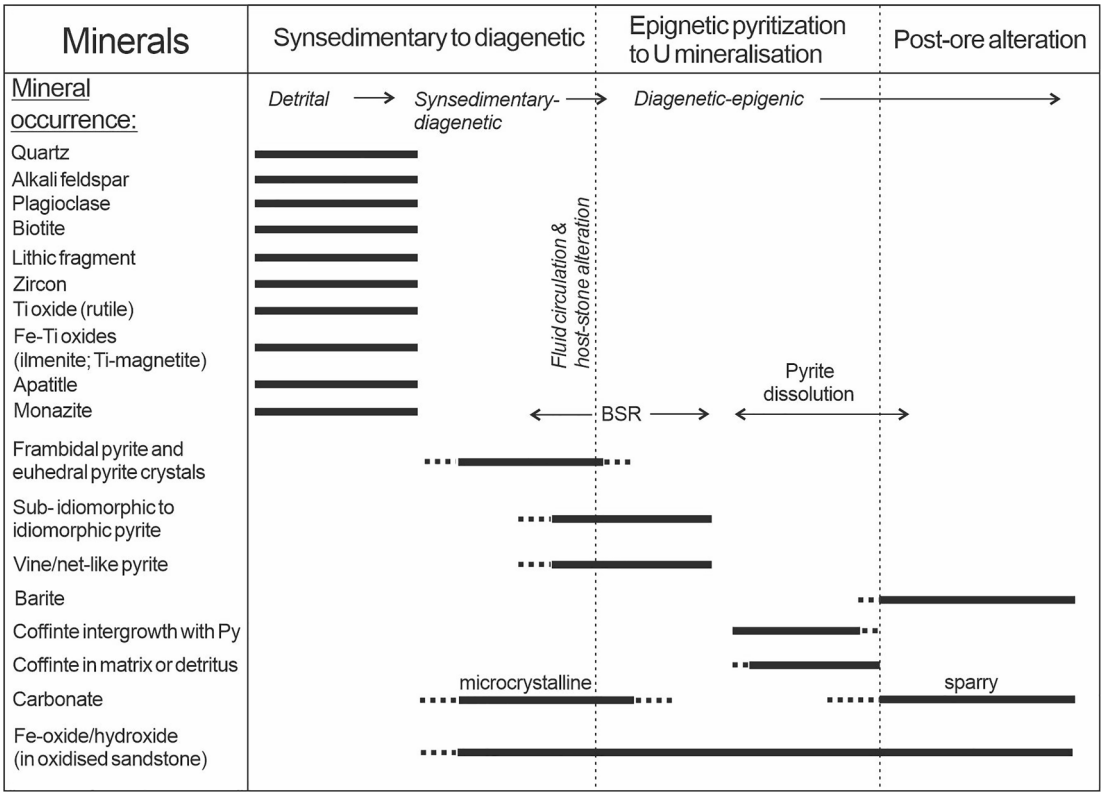


Fig. 13. The sequence of mineral paragenesis of the Beisantai deposit.

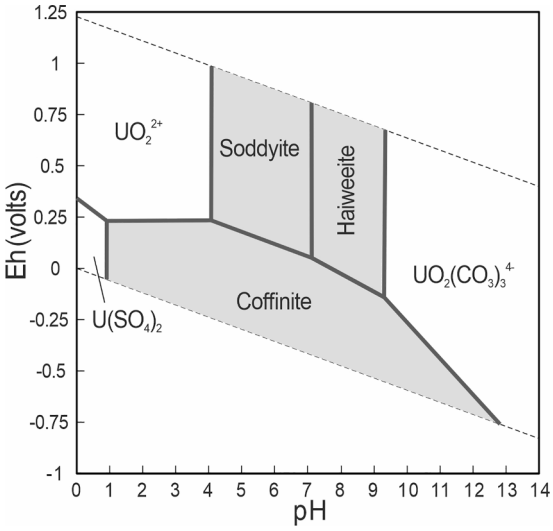


Fig.14. Solution chemistry of uranium species as a function of pH/Eh. Calculations and images were created in Geochemist's Workbench® (thermo.dat database) (Bethke, 2014) using the following condition: concentration U 10^{-6} M: P_{CO2} $10^{-3.5}$; at 1/100 seawater concentration at 25 °C; and increased concentrations of SiO_4^{4+} (Modified after Cumberland et al., 2016).

the environment has changed greatly, leading to the uranium precipitation through appropriate Physico-chemical reactions. Indeed, the mineralization processes are far more complex than the simple reduction of U(VI) to U(IV) but involve multiple interactions among fluids of different properties and various minerals.

As demonstrated above, the infiltrated groundwater is characterized by oxidising and alkaline, with carbonate ions dissolved. This downward fluid has first leached uranium from outcropping source rocks migrated along with the permeable conglomerates or sandstones, which led to the oxidation of pre-ore pyrite and the partial liberating of uranium in unstable minerals. Unstable silicate minerals also supplied a source of Si (Cai et al., 2007a, b). In the solution, uranium readily forms carbonate complexes such as $[UO_2(CO_3)_2]^{2-}$ and $[UO_2(CO_3)_3]^{4-}$ (Fig. 15; Nash et al., 1981, Cumberland et al., 2016) for the strong affinity of U to carbonates (Behrends and Van Cappellen, 2005; Cheng et al., 2012). On contrast, the formation is in an acidic environment, in which pyrites dissolution creates a lot of local acidic and reducing centers favorable for uranium precipitation. It can rationally speculate that when the two fluids mix, both the mobility and stability of uranyl carbonate complexes and silicate in the ore-bearing solution decrease abruptly as the sudden decrease in pH. Simultaneously, stable uranyl carbonate complexes

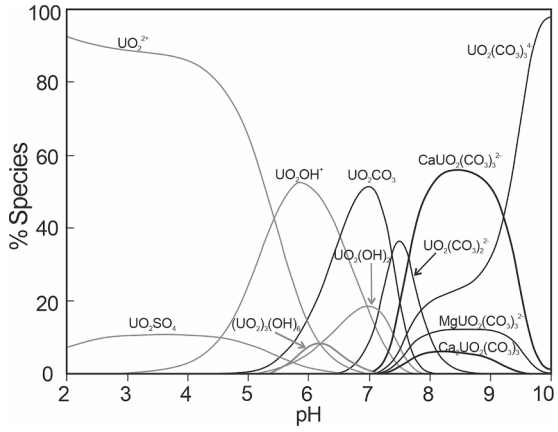


Fig. 15. Relative concentration of uranyl complexes for UO_2-H_2O-CO_2 system under the following condition: concentration U 10^{-6} M: P_{CO2} $10^{-3.5}$; at 1/100 seawater concentration at 25 °C (Modified after Cumberland et al., 2016). Modelled speciation generated using PHREEQC (Parkhurst, 1995).

break down into free uranyl ions that are readily to be adsorbed (Bachmaf and Merkel, 2010; Li et al., 2013) and reduced (Hua et al., 2006; Kelly et al., 2006; Stewart et al., 2010). Under the promotion of microbes, coffinite deposits dominantly through the reduction of pyrite. Therefore, the mixing of infiltrated alkaline fluids and internal acidic reducing fluids contributes significantly to uranium mineralization.

6. Conclusions

In the Beisantai uranium deposit, diagenetic microcrystalline calcite cement and epigenetic sparry cement dominantly occur in the redox transition zone and the oxidation zone, respectively. The broad heterogeneity of $\delta^{13}C$ values, ranging from −29.2‰ to −6.52‰, indicates the mixed sources of carbon. The strongly negative isotopic signatures in the transition zone suggest the great contributions of extrinsic hydrocarbons for the lack of indigenous organic matter in sediments. The fluid in the formation is weakly acidic, manifested by the widespread dissolution of microcrystalline calcite. The increased heavy carbon isotopic signature in the oxidation zone is attributed to the infiltrated groundwater characterized as alkaline, with carbonate dissolved. The mixture of two fluids contributes significantly to uranium mineralization.

Pyrites in the ore-bearing rock, with extremely negative $\delta^{34}S$ values (from −48.38‰ to −35.65‰), are formed through bacterial sulfate reduction. Combining the morphology features, distribution patterns, and the geochemical characteristics between individual pyrites and ore-related pyrites, a successive process of pyritization can be revealed. The pyritization has lasted a relatively short period and ceased before the ore stage due to the consumption of organic matter as well as the decline of sulfate-reducing bacteria. Pyrite is the predominant reductant for the precipitation of coffinite, with the catalysis and acceleration of microbes.

Declaration of Competing Interest

The authors declare that they have no known competing financial interests or personal relationships that could have appeared to influence the work reported in this paper.

Acknowledgements

This study is supposed by National Key R & D program of China (No. 2018YFC0604200) from the Ministry of Science and Technology, China; the National Natural Science Foundation of China (Grants No.42102069); and the International Geoscience Programme (IGCP-675). Special thanks to Tianjin Center, China Geological Survey; China Coal Geology Group CO., Ltd; and Xinjiang Oilfield Company, PetroChina for their assistance in sampling. We are particularly grateful to the anonymous reviewers for their constructive comments that have helped to significantly improve the quality of the manuscript. We also thank editorial employees for editing the manuscript.

References

Abdelouas, A., Lu, Y., Lutze, W., Nuttall, H.E., 1998. Reduction of U (VI) to U (IV) by indigenous bacteria in contaminated ground water. J. Contam. Hydrol. 35 (1-3), 217–233.

Akhtar, S., Yang, X., Pirajno, F., 2017. Sandstone type uranium deposits in the Ordos Basin, Northwest China: A case study and an overview. J. Asian Earth Sci. 146, 367–382.

Alessi, D.S., Lezama-Pacheco, J.S., Stubbs, J.E., Janousch, M., Bargar, J.R., Persson, P., Bernier-Latmani, R., 2014. The product of microbial uranium reduction includes multiple species with U (IV)–phosphate coordination. Geochim. Cosmochim. Acta 131, 115–127.

Allen, M.B., ªEngör, A.M.C., Natal'in, B.A., 1995. Junggar, Turfan and Alakol basins as Late Permian to ?Early Triassic extensional structures in a sinistral shear zone in the Altaid orogenic collage, Central Asia. Journal of the Geological Society. 152 (2), 327–338.

Amrhein, C., Mosher, P.A., Brown, A.D., 1993. The effects of redox on Mo, U, B, V, and As solubility in evaporation pond soils. Soil Sci. 155 (4), 249–255.

Aplin, A.C., Coleman, M.L., 1995. Sour gas and water chemistry of the Bridport Sands reservoir, Wytch Farm, UK. Geol. Soc. London Spec. Publ. 86 (1), 303–314.

Bachmaf, S., Merkel, B. J., 2010. Sorption and desorption of uranium (VI) on clay minerals.

Bao, Z., Chen, L.u., Zong, C., Yuan, H., Chen, K., Dai, M., 2017. Development of pressed sulfide powder tablets for in situ sulfur and lead isotope measurement using LA-MC-ICP-MS. Int. J. Mass Spectrom. 421, 255–262.

Barton, L.L., Goulhen, F., Bruschi, M., Woodards, N.A., Plunkett, R.M., Rietmeijer, F.J.M., 2007. The bacterial metallome: composition and stability with specific reference to the anaerobic bacterium Desulfovibrio desulfuricans. Biometals 20 (3-4), 291–302.

Behrends, T., Van Cappellen, P., 2005. Competition between enzymatic and abiotic reduction of uranium (VI) under iron reducing conditions. Chem. Geol. 220 (3-4), 315–327.

Belyi, V.M., Vinogradov, V.I., Lisitsin, A.K., 1972. Sulfur isotope composition of uranium roll ore bodies and its genetic significance. Litologiya i Poleznye Iskopaemye. 6, 42–53.

Bethke, 2014. The geochemist's workbench. Release 10.0. GWB essentials guide.

Bonnetti, C., Liu, X., Zhaobin, Y., Cuney, M., Michels, R., Malartre, F., Mercadier, J., Cai, J., 2017. Coupled uranium mineralisation and bacterial sulphate reduction for the genesis of the Baxingtu sandstone-hosted U deposit, SW Songliao Basin, NE China. Ore Geol. Rev. 82, 108–129.

Bonnetti, C., Cuney, M., Michels, R., Truche, L., Malartre, F., Liu, X., Yang, J., 2015. The multiple roles of sulfate-reducing bacteria and Fe-Ti oxides in the genesis of the Bayinwula roll front-type uranium deposit, Erlian Basin, NE China. Econ. Geol. 110 (4), 1059–1081.

Bonnetti, C., Zhou, L., Riegler, T., Brugger, J., Fairclough, M., 2020. Large S isotope and trace element fractionations in pyrite of uranium roll front systems result from internally-driven biogeochemical cycle. Geochim. Cosmochim. Acta 282, 113–132.

Boon, M., Brasser, H.J., Hansford, G.S., Heijnen, J.J., 1999. Comparison of the oxidation kinetics of different pyrites in the presence of Thiobacillus ferrooxidans or Leptospirillum ferrooxidans. Hydrometallurgy 53 (1), 57–72.

Borch, T., Roche, N., Johnson, T.E., 2012. Determination of contaminant levels and remediation efficacy in groundwater at a former in situ recovery uranium mine. J. Environ. Monit. 14 (7), 1814. https://doi.org/10.1039/c2em30077j.

Børresen, H. S. Geochemical and mineralogical evaluation of mineral-water reactions and leaching potential in a black shale depot-Weathering and transport of Ni, Zn, Cd, Sr and Co from Alum-and Black shale: 2017.

Botsou, F., Godelitsas, A., Kaberi, H., Mertzimekis, T.J., Goettlicher, J., Steininger, R., Scoullos, M., 2015. Distribution and partitioning of major and trace elements in pyrite-bearing sediments of a Mediterranean coastal lagoon. Geochemistry 75 (2), 219–236.

Brunner, B., Bernasconi, S.M., 2005. A revised isotope fractionation model for dissimilatory sulfate reduction in sulfate reducing bacteria. Geochim. Cosmochim. Acta 69 (20), 4759–4771.

Cai, C., Dong, H., Li, H., Xiao, X., Ou, G., Zhang, C., 2007a. Mineralogical and geochemical evidence for coupled bacterial uranium mineralization and hydrocarbon oxidation in the Shashagetai deposit. NW China. Chemical Geology. 236 (1-2), 167–179.

Cai, C., Li, H., Qin, M., Luo, X., Wang, F., Ou, G., 2007b. Biogenic and petroleum-related ore-forming processes in Dongsheng uranium deposit, NW China. Ore Geol. Rev. 32 (1-2), 262–274.

Cai, C., Worden, R.H., Wang, Q., Xiang, T., Zhu, J., Chu, X., 2002. Chemical and isotopic evidence for secondary alteration of natural gases in the Hetianhe Field, Bachu Uplift of the Tarim Basin. Org Geochem. 33 (12), 1415–1427.

Cai, Z.X., Chen, F.J., Jia, Z.Y., 2000. Types and tectonic evolution of Junggar Basin. Earth Sci. Front. (China University of Geosciences, Beijing). 7–4, 431–440 (in Chinese with an English abstract).

Carroll, A.R., Yunhai, L., Graham, S.A., Xuchang, X., Hendrix, M.S., Jinchi, C., McKnight, C.L., 1990. Junggar basin, northwest China: trapped Late Paleozoic ocean. Tectonophysics 181 (1-4), 1–14.

Chen, X., Lu, H.F., Shu, L.S., Wang, H.M., Zhang, G.Q., 2002. Study on Tectonic Evolution of Junggar Basin. Geol. J. China Univ. 8–3, 257–267 (in Chinese with an English abstract).

Chen, Y., Jin, R., Miao, P., Li, J., Guo, H.u., Chen, L., 2019. Occurrence of pyrites in sandstone-type uranium deposits: Relationships with uranium mineralization in the North Ordos Basin, China. Ore Geol. Rev. 109, 426–447.

Chen, Z.Y., Guo, Q.Y., 2007. Mechanism of U-reduction and concentration by sulphides at sandstone type uranium deposits. Uranium Geol. 23–6 (321–327), 334 (in Chinese with an English abstract).

Cheng, Y., Holman, H.-Y., Lin, Z., 2012. Remediation of chromium and uranium contamination by microbial activity. Elements. 8 (2), 107–112.

Crundwell, F.K., 2003. How do bacteria interact with minerals? Hydrometallurgy 71 (1-2), 75–81.

Cumberland, S.A., Douglas, G., Grice, K., Moreau, J.W., 2016. Uranium mobility in organic matter-rich sediments: A review of geological and geochemical processes. Earth Sci. Rev. 159, 160–185.

Curiale, J.A., Bloch, S., Rafalska-Bloch, J., Harrison, W.E., 1983. Petroleum-related origin for uraniferous organic-rich nodules of southwestern Oklahoma. AAPG Bull. 67–4, vii.

Demaison, G.J., Hoick, A.J.J., Jones, R.W., Moore, G.T., 1983. Predictive source bed stratigraphy; a guide to regional petroleum occurrence. In: Proceedings of the 11th World Petroleum Congress, London, vol. 2, pp. 17–29.

Diehl, S.F., Goldhaber, M.B., Koenig, A.E., Lowers, H.A., Ruppert, L.F., 2012. Distribution of arsenic, selenium, and other trace elements in high pyrite Appalachian coals: evidence for multiple episodes of pyrite formation. Int. J. Coal Geol. 94, 238–249.

Dopson, M., Baker-Austin, C., Koppineedi, P.R., Bond, P.L., 2003. Growth in sulfidic mineral environments: metal resistance mechanisms in acidophilic micro-organisms. Microbiology 149–8, 1959–1970.
Dungan, R.S., Frankenberger, W.T., 1999. Microbial transformations of selenium and the bioremediation of seleniferous environments. Biorem. J. 3 (3), 171–188.
Edman, J.D., Surdam, R.C., 1986. Organic-inorganic interactions as a mechanism for porosity enhancement in the Upper Cretaceous Ericson Sandstone, Green River Basin, Wyoming. The Society of Economic Paleontologists and Mineralogists Roles of Organic Matter in Sediment Diagenesis.
Eglizaud, N., Miserque, F., Simoni, E., Schlegel, M., Descostes, M., 2006. Uranium (VI) interaction with pyrite (FeS2): Chemical and spectroscopic studies. Radiochim. Acta 94–9, 651–656.
Espitalie, J., Deroo, G., Marquis, F., 1985. Rock-Eval pyrolysis and its applications (part one). Oil Gas Sci. Technol.-Revue d'IFPEN. 40–5, 563–579.
Feng, M.-H., Ngwenya, B.T., Wang, L., Li, W., Olive, V., Ellam, R.M., 2011. Bacterial dissolution of fluorapatite as a possible source of elevated dissolved phosphate in the environment. Geochim. Cosmochim. Acta 75 (19), 5785–5796.
Fowler, T.A., Holmes, P.R., Crundwell, F.K., 2001. On the kinetics and mechanism of the dissolution of pyrite in the presence of Thiobacillus ferrooxidans. Hydrometallurgy 59 (2-3), 257–270.
Friedman, I., O'Neil, J.R., 1977. Compilation of stable isotope fractionation factors of geochemical interest: US Government Printing. Office.
Gächter, R., Meyer, J.S., 1993. The role of microorganisms in mobilization and fixation of phosphorus in sediments. In: Proceedings of the Third International Workshop on Phosphorus in Sediments. Springer Netherlands, Dordrecht, pp. 103–121.
Gallegos, T.J., Campbell, K.M., Zielinski, R.A., Reimus, P.W., Clay, J.T., Janot, N., Bargar, J.R., Benzel, W.M., 2015. Persistent U(IV) and U(VI) following in-situ recovery (ISR) mining of a sandstone uranium deposit, Wyoming, USA. Appl. Geochem. 63, 222–234.
Gargarello, R.M., Di Gregorio, D., Huck, H., Fernandez Niello, J., Curutchet, G., 2009. Aerobic reduction of uranium(VI) by acidithiobacillus thiooxidans cultures. Adv. Mater. Res. 71–73, 641–644.
Gargarello, R.M., Di Gregorio, D., Huck, H., Fernandez Niello, J., Curutchet, G., 2010. Reduction of uranium(VI) by Acidithiobacillus thiooxidans and Acidithiobacillus ferrooxidans. Hydrometallurgy 104 (3-4), 529–532.
Gleisner, M., Herbert, R.B., Frogner Kockum, P.C., 2006. Pyrite oxidation by Acidithiobacillus ferrooxidans at various concentrations of dissolved oxygen. Chem. Geol. 225 (1-2), 16–29.
Goldhaber, M.B., Hemingway, B.S., Mohagheghi, A., Reynolds, R.L., Northrop, H.R., 1987. Origin of coffinite in sedimentary rocks by a sequential adsorption-reduction mechanism. Bull. Minér. 110 (2), 131–144.
Granger, H. C., Warren, C. G. Zoning in the altered tongue associated with roll-type uranium deposits. Formation of uranium ore deposits1974.
Griffin, W. L., 2008. GLITTER: data reduction software for laser ablation ICP-MS. Laser Ablation ICP-MS in the Earth Sciences: Current practices and outstanding issues. 308-311.
Habicht, K.S., Canfield, D.E., 1997. Sulfur isotope fractionation during bacterial sulfate reduction in organic-rich sediments. Geochim. Cosmochim. Acta 61 (24), 5351–5361.
Hansley, P. L., Spirakis, C. S., 1992. Organic matter diagenesis as the key to a unifying theory for the genesis of tabular uranium-vanadium deposits in the Morrison Formation, Colorado Plateau. Economic Geology. 87-2, 352-365.
Herbin, J.P., Deroo, G., 1979. Etude sédimentologique de la matière organique dans les argiles noires. Crétacées de l'Atlantique sud 75, 71–87.
Hoefs, J., 2015. Stable Isotope Geochemistry. Springer International Publishing, Cham.
Hu, X.W., Yang, X.Y., Ren, Y.S., Wu, Z.J., Du, G.F., Huang, T.T., 2020. Sedimentary environment and tectonic evolution of Junggar Basin: Constrains on the mineralization of sandstone-type uranium deposits. Geotect. Metall. 44–4, 725–741 (in Chinese with an English abstract).
Hua, B., Xu, H., Terry, J., Deng, B.L., 2006. Kinetics of uranium(VI) reduction by hydrogen sulfide in anoxic aqueous systems. Environ. Sci. Technol. 40 (15), 4666–4671.
Hutchens, E., Valsami-Jones, E., Harouiya, N., Chaïrat, C., Oelkers, E.H., McEldoney, S., 2006. An experimental investigation of the effect of Bacillus megaterium on apatite dissolution. Geomicrobiol J. 23 (3-4), 177–182.
Ingham, E.S., Cook, N.J., Cliff, J., Ciobanu, C.L., Huddleston, A., 2014. A combined chemical, isotopic and microstructural study of pyrite from roll-front uranium deposits, Lake Eyre Basin, South Australia. Geochim. Cosmochim. Acta 125, 440–465.
Jaireth, S., McKay, A., Lambert, I., 2008. Association of large sandstone uranium deposits with hydrocarbons. Australian Goverment Geoscience Australia. 89-6, 1-6.
Jensen, M. L., 1958. Sulfur isotopes and the origin of sandstone-type uranium deposits [Colorado Plateau and Wyoming]. Economic Geology. 53-5, 598-616.
Jiang, L., 2006. Bio-oxidation of pyrite, chalcopyrite, pyrrhotite and galena by Acidithiobacillus ferrooxidans. Gradute School of the Chinese Academy of Sciences, Guangzhou (in Chinese with an English abstract).
Jiang, L., Yang, H., Tao, Y., Yang, J., 2011. Pyrite surface corrosion enhanced by attachment of Acidithiobacillus ferrooxidans: comparison with abiotic oxidation. Environ. Eng. Manage. J. (EEMJ). 10 (6), 819–823.
Jin, R., Yu, R.-A., Yang, J., Zhou, X., Teng, X., Wang, S., Si, Q., Zhu, Q., Zhang, T., 2019. Paleo-environmental constraints on uranium mineralization in the Ordos Basin: Evidence from the color zoning of U-bearing rock series. Ore Geol. Rev. 104, 175–189.
Jones, R.A., Koval, S.F., Nesbitt, H.W., 2003. Surface alteration of arsenopyrite (FeAsS) by Thiobacillus ferrooxidans. Geochim. Cosmochim. Acta 67 (5), 955–965.
Kaplan, I.R., Rittenberg, S.C., 1964. Microbiological Fractionation of Sulphur Isotopes. J. Gen. Microbiol. 34 (2), 195–212.
Kelly, S.D., Rasbury, E.T., Chattopadhyay, S., Kropf, A.J., Kemner, K.M., 2006. Evidence of a stable uranyl site in ancient organic-rich calcite. Environ. Sci. Technol. 40 (7), 2262–2268.
Knoblauch, C., Jorgensen, B.B., 1999. Effect of temperature on sulphate reduction, growth rate and growth yield in five psychrophilic sulphate-reducing bacteria from Arctic sediments. Environ. Microbiol. 1 (5), 457–467.
Kusebauch, C., Oelze, M., Gleeson, S.A., 2018. Partitioning of arsenic between hydrothermal fluid and pyrite during experimental siderite replacement. Chem. Geol. 500, 136–147.
Kyser, K., 2014. Uranium ore deposits. In: Treatise on Geochemistry, second ed., pp. 489–513.
Kyser, K., 2016. Exploration for uranium. In: Uranium for Nuclear Power. Elsevier, pp. 53–76.
Larson, L.N., Kipp, G.G., Mott, H.V., Stone, J.J., 2012. Sediment pore-water interactions associated with arsenic and uranium transport from the North Cave Hills mining region, South Dakota, USA. Appl. Geochem. 27 (4), 879–891.
Le Pape, P., Blanchard, M., Brest, J., Boulliard, J.-C., Ikogou, M., Stetten, L., Wang, S., Landrot, G., Morin, G., 2017. Arsenic incorporation in pyrite at ambient temperature at both tetrahedral S-I and octahedral FeII sites: Evidence from EXAFS–DFT analysis. Environ. Sci. Technol. 51 (1), 150–158.
Leibold, J., 2013. Geochemistry and mineralogy of the alteration halo associated with the Three Crow roll-front uranium deposit, Nebraska. Colorado School of Mines, USA.
Li, J., Pang, Z.H., Froehlich, K., Huang, T.M., Kong, Y., Song, W.H., Yun, H.X., 2015. Paleo-environment from isotopes and hydrochemistry of groundwater in East Junggar Basin, Northwest China. Journal of Hydrology. 529, 650–661.
Li, X., Wu, J., Liao, J., Zhang, D., Yang, J., Feng, Y., Zeng, J., Wen, W., Yang, Y., Tang, J., Liu, N., 2013. Adsorption and desorption of uranium (VI) in aerated zone soil. J. Environ. Radioact. 115, 143–150.
Liao, J.D., Liu, C.M., Cheng, X.S., Song, Y.L., Guo, Y.X., Wang, H.J., 2002. Geochemistry of oil reservoirs in Santai and Beisantai oilfilds. Junggar Basin. Xinjiang Geology. 20–3, 247–251 (in Chinese with an English abstract).
Liu, C.W., Guo, X.G., Wang, Z.S., Zhu, L.L., Zhang, R., Chen, H., 2020a. Study on hydrocarbon accumulation stage of Jurassic Toutunhe Formation in Fudong Slope. Junggar Basin. Natural Gas Geoscience. 20–3, 247–251 (in Chinese with an English abstract).
Liu, G., Zeng, L., Wang, X., Ostadhassan, M., Wang, Z., Mao, Z., Tie, Q.i., 2020b. Natural fractures in deep tight gas sandstone reservoirs in the thrust belt of the southern Junggar Basin, northwestern China. Interpretation. 8 (4), SP81–SP93.
Liu, W., Zhang, X.L., 2011. Evidence for microbial dissolution of pyrite from the Lower Cambrian oolitic limestone, South China. Biogeosci. Discuss. 8–2, 2035–2056.
Lovley, D.R., Phillips, E.J., 1992. Reduction of uranium by Desulfovibrio desulfuricans. Appl. Environ. Microbiol. 58 (3), 850–856.
Lovley, D.R., Phillips, E.J.P., Gorby, Y.A., Landa, E.R., 1991. Microbial reduction of uranium. Nature 350 (6317), 413–416.
Lovley, D.R., Roden, E.E., Phillips, E.J.P., Woodward, J.C., 1993. Enzymatic iron and uranium reduction by sulfate-reducing bacteria. Mar. Geol. 113 (1-2), 41–53.
Luo, B.W., Zhang, G.Y., Wei, Y.Z., Liu, L., Zhao, X., Zhang, X.G., 2012. Analysis of the Late Carboniferous prototype basin in the Ludong-Wucaiwan area of the Junggar Basin. Chin. J. Geol. 47–3, 685–699 (in Chinese with an English abstract).
Ma, B., Fernandez-Martinez, A., Kang, M., Wang, K., Lewis, A.R., Maffeis, T.G.G., Findling, N., Salas-Colera, E., Tisserand, D., Bureau, S., Charlet, L., 2020. Influence of surface compositions on the reactivity of pyrite toward aqueous U (VI). Environ. Sci. Technol. 54 (13), 8104–8114.
Machel, H.G., 2001. Bacterial and thermochemical sulfate reduction in diagenetic settings—old and new insights. Sed. Geol. 140 (1-2), 143–175.
Mercadier, J., Cuney, M., Cathelineau, M., Lacorde, M., 2011. U redox fronts and kaolinisation in basement-hosted unconformity-related U ores of the Athabasca Basin (Canada): late U remobilisation by meteoric fluids. Miner. Deposita 46 (2), 105–135.
Miao, A.S., Qi, L.U., Liu, H.F., Xiao, P., 2010. Electronic Microscopy Study on the Uranium Minerals of Dongsheng Sandstone-type Uranium Deposit in Ordos Basin. Geoscience. 24–4, 785–792 (in Chinese with an English abstract).
Min, M., Chen, J., Wang, J., Wei, G., Fayek, M., 2005a. Mineral paragenesis and textures associated with sandstone-hosted roll-front uranium deposits, NW China. Ore Geol. Rev. 26 (1-2), 51–69.
Min, M., Xu, H., Chen, J., Fayek, M., 2005b. Evidence of uranium biomineralization in sandstone-hosted roll-front uranium deposits, northwestern China. Ore Geol. Rev. 26 (3-4), 198–206.
Moosa, S., Nemati, M., Harrison, S.T.L., 2005. A kinetic study on anaerobic reduction of sulphate, part II: incorporation of temperature effects in the kinetic model. Chem. Eng. Sci. 60 (13), 3517–3524.
Mustin, C., Berthelin, J., Marion, P., de Donato, P., 1992. Corrosion and electrochemical oxidation of a pyrite by Thiobacillus ferrooxidans. Appl. Environ. Microbiol. 58 (4), 1175–1182.
Nash, J.T., Granger, H.C., Adams, S.S., 1981. Geology and concepts of genesis of important types of uranium deposits. Econ. Geol. 63–116.
OECD-NEA/IAEA, 2020, Uranium 2020: Resources, production and demand.
Pan, F.Y., 2007. Hydrocarbon indicator significance of organic inclusions in the Jurassic reservoirs in Beisantai area of Junggar Basin. Xinjiang Oil & Gas. 3–3, 11–15 (in Chinese with an English abstract).
Parkhurst, D.L., 1995. User guide to PHREEQC - A computer program for speciation, reactionpath, advective-transport, and inverse geochemical calculations. Center for Integrated Data Analytics Wisconsin Science Center.

Pearce, N.J.G., Perkins, W.T., Westgate, J.A., Gorton, M.P., Jackson, S.E., Neal, C.R., Chenery, S.P., 1997. A compilation of new and published major and trace element data for NIST SRM 610 and NIST SRM 612 glass reference materials. Geostandards Newslett. 21–1, 115–144.
MIAO, P., JIN, R., LI, J., ZHAO, H., CHEN, L., CHEN, Y., SI, Q., 2020. The First Discovery of a Large Sandstone-type Uranium Deposit in Aeolian Depositional Environment. Acta Geol. Sin. (English Edition) 94 (2), 583–584.
Pisapia, Céline, Chaussidon, M., Mustin, C., Humbert, B., 2007. O and S isotopic composition of dissolved and attached oxidation products of pyrite by Acidithiobacillus ferrooxidans: comparison with abiotic oxidations. Geochim. Cosmochim. Acta 71 (10), 2474–2490.
Pisapia, Céline, Humbert, B., Chaussidon, M., Mustin, C., 2008. Perforative corrosion of pyrite enhanced by direct attachment of Acidithiobacillus ferrooxidans. Geomicrobiol J. 25 (6), 261–273.
Qafoku, N.P., Kukkadapu, R.K., McKinley, J.P., Arey, B.W., Kelly, S.D., Wang, C., Resch, C.T., Long, P.E., 2009. Uranium in framboidal pyrite from a naturally bioreduced alluvial sediment. Environ. Sci. Technol. 43 (22), 8528–8534.
Qian, G., Brugger, J., Testemale, D., Skinner, W., Pring, A., 2013. Formation of As (II)-pyrite during experimental replacement of magnetite under hydrothermal conditions. Geochim. Cosmochim. Acta 100, 1–10.
Rackley, R.I., 1972. Environment of Wyoming Tertiary uranium deposits. AAPG Bull. 56–4, 755–774.
Rallakis, D., Michels, R., Brouand, M., Parize, O., Cathelineau, M., 2019. The role of organic matter on uranium precipitation in Zoovch Ovoo, Mongolia. Minerals 9 (5), 310. https://doi.org/10.3390/min9050310.
Reynolds, R.L., Goldhaber, M.B., 1978. Origin of a South Texas roll-type uranium deposit; I, Alteration of iron-titanium oxide minerals. Econ. Geol. 73–8, 1677–1689.
Sampson, M.I., Phillips, C.V., Ball, A.S., 2000. Investigation of the attachment of Thiobacillus ferrooxidans to mineral sulfides using scanning electron microscopy analysis. Miner. Eng. 13 (6), 643–656.
Sani, R.K., Peyton, B.M., Amonette, J.E., Geesey, G.G., 2004. Reduction of uranium (VI) under sulfate-reducing conditions in the presence of Fe (III)-(hydr) oxides. Geochim. Cosmochim. Acta 68 (12), 2639–2648.
Sasaki, K., Tsunekawa, M., Ohtsuka, T., Konno, H., 1998. The role of sulfur-oxidizing bacteria Thiobacillus thiooxidans in pyrite weathering. Colloids Surf., A 133 (3), 269–278.
Scott, T.B., Riba Tort, O., Allen, G.C., 2007. Aqueous uptake of uranium onto pyrite surfaces; reactivity of fresh versus weathered material. Geochim. Cosmochim. Acta 71 (21), 5044–5053.
Seal, R.R., 2006. Sulfur Isotope Geochemistry of Sulfide Minerals. Rev. Mineral. Geochem. 61 (1), 633–677.
Sharp, Z., 2017. Principles of Stable Isotope Geochemistry, 2nd ed. Pearson Prentice Hall, New Jersey.
Southam, G., Saunders, J.A., 2005. The geomicrobiology of ore deposits. Econ. Geol. 100 (6), 1067–1084.
Spear, J.R., Figueroa, L.A., Honeyman, B.D., 1999. Modeling the removal of uranium U (VI) from aqueous solutions in the presence of sulfate reducing bacteria. Environ. Sci. Technol. 33 (15), 2667–2675.
Spirakis, C.S., 1996. The roles of organic matter in the formation of uranium deposits in sedimentary rocks. Ore Geol. Rev. 11 (1-3), 53–69.
Stewart, B.D., Mayes, M.A., Fendorf, S., 2010. Impact of uranyl− calcium− carbonato complexes on uranium (VI) adsorption to synthetic and natural sediments. Environ. Sci. Technol. 44 (3), 928–934.
Sun, W.J., Zhao, S.J., Li, S.Z., Suo, Y.H., Liu, X., Lou, D., Yu, S., Yang, Z., Wang, X.B., Li, T., 2014. Mesozoic Tectonic Migration in the Eastern Junggar Basin. Geotectonica et Metallogenia. 38–1, 52–61 (in Chinese with an English abstract).
Szenknect, S., Mesbah, A., Cordara, T., Clavier, N., Brau, H.-P., Le Goff, X., Poinssot, C., Ewing, R.C., Dacheux, N., 2016. First experimental determination of the solubility constant of coffinite. Geochim. Cosmochim. Acta 181, 36–53.
Teclu, D., Tivchev, G., Laing, M., Wallis, M., 2008. Bioremoval of arsenic species from contaminated waters by sulphate-reducing bacteria. Water Res. 42 (19), 4885–4893.
Toniazzo, V., Lazaro, I., Humbert, B., Mustin, C., 1999. Bioleaching of pyrite by Thiobacillus ferrooxidans: fixed grains electrode to study superficial oxidized compounds. Comptes Rendus de l'Académie des Sciences-Series IIA-Earth Planet. Sci. 328 (8), 535–540.
Ulrich, K.-U., Veeramani, H., Bernier-Latmani, R., Giammar, D.E., 2011. Speciation-dependent kinetics of uranium(VI) Bioreduction. Geomicrobiol. J. 28 (5-6), 396–409.
Wang, Y.T., Chen, K.X., 1990. Affinities between crude oils and thermal evolution histories of source beds, Santai-North Santai Area, junggar Basin. Xinjiang Petrol. Geol. 11–1, 50–58 (in Chinese with an English abstract).
Wei, H., Wei, X., Qiu, Z., Song, H., Shi, G., 2016. Redox conditions across the G-L boundary in South China: Evidence from pyrite morphology and sulfur isotopic compositions. Chem. Geol. 440, 1–14.
Wersin, P., Hochella, M.F., Persson, P., Redden, G., Leckie, J.O., Harris, D.W., 1994. Interaction between aqueous uranium (VI) and sulfide minerals: spectroscopic evidence for sorption and reduction. Geochim. Cosmochim. Acta 58 (13), 2829–2843.
Wignall, P.B., Védrine, S., Bond, D.P.G., Wang, W., Lai, X.-L., Ali, J.R., Jiang, H.-S., 2009. Facies analysis and sea-level change at the Guadalupian-Lopingian Global Stratotype (Laibin, South China), and its bearing on the end-Guadalupian mass extinction. J. Geol. Soc. 166 (4), 655–666.
Wilson, S.A., Ridley, W.I., Koenig, A.E., 2002. Development of sulfide calibration standards for the laser ablation inductively-coupled plasma mass spectrometry technique. J. Anal. At. Spectrom. 17 (4), 406–409.
Wu, K.Y., Zha, M., Qu, J.X., Tian, H., 2004. Control of Bogeda mountain uplift on the structural formation and evolution in Beisantai region. J. Univer. Petrol., China. 28–2, 1–5 (in Chinese with an English abstract).
Wu, Q.F., 1986. Structural evolution and prospects of Junggar Basin. Xinjiang Geology. 4–3, 1–19 (in Chinese with an English abstract).
Wu, W.-M., Carley, J., Gentry, T., Ginder-Vogel, M.A., Fienen, M., Mehlhorn, T., Yan, H., Caroll, S., Pace, M.N., Nyman, J., Luo, J., Gentile, M.E., Fields, M.W., Hickey, R.F., Gu, B., Watson, D., Cirpka, O.A., Zhou, J., Fendorf, S., Kitanidis, P.K., Jardine, P.M., Criddle, C.S., 2006. Pilot-scale in situ bioremedation of uranium in a highly contaminated aquifer. 2. Reduction of U (VI) and geochemical control of U (VI) bioavailability. Environ. Sci. Technol. 40 (12), 3986–3995.
Wu, W.-M., Carley, J., Luo, J., Ginder-Vogel, M.A., Cardenas, E., Leigh, M.B., Hwang, C., Kelly, S.D., Ruan, C., Wu, L., Van Nostrand, J., Gentry, T., Lowe, K., Tonia Mehlhorn,, Carroll, S., Luo, W., Fields, M.W., Gu, B., Watson, D., Kemner, K.M., Marsh, T., Tiedje, J., Zhou, J., Fendorf, S., Kitanidis, P.K., Jardine, P.M., Criddle, C.S., 2007. In situ bioreduction of uranium (VI) to submicromolar levels and reoxidation by dissolved oxygen. Environ. Sci. Technol. 41 (16), 5716–5723.
Wu, X.Z., Zhou, L., Yang, D.S., Qi, X.F., Li, B.H., 2012. Structure evolution and hydrocarbon accumulation the Beisantai uplift in Junggar Basin. Chin. J. Geol. 47–3, 653–668 (in Chinese with an English abstract).
Xiao, W., Han, C., Yuan, C., Sun, M., Lin, S., Chen, H., Li, Z., Li, J., Sun, S., 2008. Middle Cambrian to Permian subduction-related accretionary orogenesis of Northern Xinjiang, NW China: implications for the tectonic evolution of central Asia. J. Asian Earth Sci. 32 (2-4), 102–117.
Yang, H.B., Chen, L., Kong, Y.H., 2004. A Novel Classification of Structural Units in Junggar Basin. Xinjiang Petrol. Geol. 25–6, 686–688 (in Chinese with an English abstract).
Yang, Y., He, Z.B., 2016. Characteristics of Mesozoic-Cenozoic paleoclimate evolution and its constraint on mineralization of sandstone type uranium deposit in Junggar Basin, Xinjiang, China. World Nuclear Geosci. 33–3, 140–145 (in Chinese with an English abstract).
Yang, Y.-T., Song, C.-C., He, S., 2015. Jurassic tectonostratigraphic evolution of the Junggar basin, NW China: A record of Mesozoic intraplate deformation in Central Asia. Tectonics 34 (1), 86–115.
Yin, L., Yang, H.Y., Lu, L.S., Sand, W., Tong, L.L., Chen, G.B., Zhao, M.M., 2020. Interfacial alteration of pyrite caused by bioleaching. Hydrometallurgy 195, 105356. https://doi.org/10.1016/j.hydromet.2020.105356.
Yu, J.-Y., McGenity, T.J., Coleman, M.L., 2001. Solution chemistry during the lag phase and exponential phase of pyrite oxidation by Thiobacillus ferrooxidans. Chem. Geol. 175 (3-4), 307–317.
Yue, L., Jiao, Y., Wu, L., Rong, H., Fayek, M., Xie, H., 2020. Evolution and origins of pyrite in sandstone-type uranium deposits, northern Ordos Basin, north-central China, based on micromorphological and compositional analysis. Ore Geol. Rev. 118, 103334. https://doi.org/10.1016/j.oregeorev.2020.103334.
Yue, L., Jiao, Y., Wu, L., Rong, H., Xie, H., Wang, Q., Yan, Q., 2019. Selective crystallization and precipitation of authigenic pyrite during diagenesis in uranium reservoir sandbodies in Ordos Basin. Ore Geol. Rev. 107, 532–545.
Zhang, H., Yu, W.T., Luo, M.B., Xu, Z.L., Wu, H., 2020. Effects of Microbes and organics in the Environment on the Reduction of U(Vl) by Pyrite. Chemistry 83–2, 167–171 (in Chinese with an English abstract).
Zhang, L.C., Wu, K.Y., He, W.J., Chen, H., Zheng, M.L., Jia, X.Y., 2018. Structural characteristics and diagenetic sealing of faults in the Beisantai swell, Junggar Basin. J. Geomech. 24–5, 607–616 (in Chinese with an English abstract).
Zhang, R., 2016. Oil-source correlations and hydrocarbon accumulations of carboniferous-permian in eastern fukang depression. China University of Petroleum, Qingdao (in Chinese with an English abstract).
Zhao, L., Cai, C., Jin, R., Li, J., Li, H., Wei, J., Guo, H., Zhang, B., 2018. Mineralogical and geochemical evidence for biogenic and petroleum-related uranium mineralization in the Qianjiadian deposit, NE China. Ore Geol. Rev. 101, 273–292.
Zhao, L., Dong, T.X., Cai, C.F., Jin, R.S., Jiang, T.T., Wei, J.L., Du, H.M., Li, J.G., 2020. A review of Microbial mineralizationin Sandstone-hosted uranium deposit. Acta Geol. Sin. 94–12, 3523–3543 (in Chinese with an English abstract).
Zhao, W.J., Zhou, J.C., Yin, X.J., Hou, H.J., Yu, H.Y., 2016. Analysis about the characteristics of shallow oil and gas and favorable exploration area in Beisantai Uplift. Offshore Oil. 36–1, 23–27 (in Chinese with an English abstract).
Zhao, X., Wang, R., Lu, X., Lu, J., Li, C., Li, J., 2013. Bioleaching of chalcopyrite by Acidithiobacillus ferrooxidans. Miner. Eng. 53, 184–192.